NASA TECHNICAL MEMORANDUM

NASA TM X-3178

NASA TM X-3178

INTEGRATION OF AFT-FUSELAGE-MOUNTED FLOW-THROUGH ENGINE NACELLES ON AN ADVANCED TRANSPORT CONFIGURATION AT MACH NUMBERS FROM 0.6 TO 1.0

Bernard J. Blaha

Lewis Research Center
Cleveland, Ohio 44135

NATIONAL AERONAUTICS AND SPACE ADMINISTRATION • WASHINGTON, D. C. • MARCH 1975

1. Report No.	2. Government Accession No.	3. Recipient's Catalog No.
NASA TM X-3178		

4. Title and Subtitle	5. Report Date
INTEGRATION OF AFT-FUSELAGE-MOUNTED FLOW-THROUGH ENGINE NACELLES ON AN ADVANCED TRANSPORT CONFIGURATION AT MACH NUMBERS FROM 0.6 TO 1.0	March 1975
	6. Performing Organization Code

7. Author(s)	8. Performing Organization Report No.
Bernard J. Blaha	E-8029
	10. Work Unit No.
	501-24

9. Performing Organization Name and Address	11. Contract or Grant No.
Lewis Research Center National Aeronautics and Space Administration Cleveland, Ohio 44135	
	13. Type of Report and Period Covered
12. Sponsoring Agency Name and Address	Technical Memorandum
National Aeronautics and Space Administration Washington, D.C. 20546	14. Sponsoring Agency Code

15. Supplementary Notes

16. Abstract

An approximately 1/30th-scale model of a CTOL aircraft designed for efficient cruise between Mach 0.9 and 0.98 was tested in the Lewis Research Center's 8- by 6-Foot Supersonic Wind Tunnel. Aft-fuselage axial force and pressure were measured for a series of locally area-ruled engine installations. Two flow-through nacelles with different exit diameters which simulated inlet mass flow ratios of 0.46 and 0.6 (based on maximum nacelle cross-sectional area) were investigated. Both an NACA-1 cowl and a blunter supercritical cowl were tested with these nacelles. Variations in the amount of local area ruling were investigated and an aft fuselage without nacelles was tested for reference. Results observed with flow-through nacelles indicate that efficient cruise may be obtained on this type of aircraft with aft-fuselage-mounted engine nacelles.

17. Key Words (Suggested by Author(s))	18. Distribution Statement
Transonic aerodynamics; Airframe integration; Subsonic nacelles; Aft-fuselage integration; Supercritical-wing transport aircraft; Advanced Technology Transport (ATT)	Unclassified - unlimited STAR Category 02 (rev.)

19. Security Classif. (of this report)	20. Security Classif. (of this page)	21. No. of Pages	22. Price*
Unclassified	Unclassified	71	$4.25

* For sale by the National Technical Information Service, Springfield, Virginia 22151

INTEGRATION OF AFT-FUSELAGE-MOUNTED FLOW-THROUGH ENGINE NACELLES ON AN ADVANCED TRANSPORT CONFIGURATION AT MACH NUMBERS FROM 0.6 TO 1.0

by Bernard J. Blaha

Lewis Research Center

SUMMARY

Tests were conducted in the Lewis Research Center's 8- by 6-Foot Supersonic Wind Tunnel to investigate the problems associated with the integration of aft-fuselage-mounted engine nacelles. An approximately 1/30th-scale full-span model of an advanced CTOL transport-type aircraft (200 passengers) designed to cruise between Mach 0.9 and 0.98 was used. The model was tested with flow-through engine nacelles to determine aft-fuselage axial force and pressures for a series of locally area-ruled installations. Two nacelles with different internal exit diameters which simulated inlet mass flow ratios of 0.46 and 0.6 were investigated. An NACA-1 cowl and a blunter supercritical cowl were also tested. Variations in local area ruling were investigated, and an aft fuselage without nacelles was tested for reference. Boundary-layer and local flow angle measurements were made near the nacelle inlet locations. Data were obtained over a Mach number range of 0.6 to 1.0, and angle of attack was varied from 0° to 4.2°.

Results observed with the flow-through nacelles indicate that efficient cruise may be obtained for this type of aircraft with aft-fuselage-mounted engine nacelles in the speed range from Mach 0.9 to nearly 0.98 at the cruise angle of attack, 3.2°. At these cruise conditions, the addition of engine nacelles to a properly contoured configuration increased the aft-fuselage axial force by only the calculated nacelle skin friction. Drag-rise Mach number was approximately 0.98 for the best nacelle configurations. A blunt inlet cowl geometry (supercritical) resulted in lower aft-fuselage pressures with correspondingly higher drag and lowered drag-rise Mach number. The effects of improper area ruling were to increase drag at the cruise speeds and to reduce drag-rise Mach number. Increased angle of attack resulted in reduced aft-fuselage axial force and increased drag-rise Mach number to the cruise angle of attack. Boundary-layer measurements indicate that the upstream model geometry had only small effects on boundary-layer profile. Local flow angles as large as 4° were measured on the reference fuselage near the inlet axial locations. Local Mach numbers measured near the inlet locations were slightly suppressed at the cruise speeds.

INTRODUCTION

Recently studies have been made to investigate the problems associated with the development of an advanced CTOL transport aircraft (~200 passengers) designed to cruise efficiently at speeds from Mach 0.9 to 0.98 (refs. 1 to 17). In addition to providing significant reductions in travel time (especially for long-range missions), the overall design objectives include reduced pollution and quieter operation. Extensive efforts have been made to develop for this cruise speed range an efficient airframe configuration which incorporates the use of the supercritical wing and area-ruling technology (refs. 1 to 7). Likewise, extensive efforts have been made in the determination of the propulsion technology requirements for this type of aircraft (refs. 8 to 14). One of the more significant problems for this type of aircraft that is presently being investigated within NASA and the aircraft industry is the integration of the propulsion system and the airframe (refs. 7, and 14 to 16). One of the major reasons present transport aircraft are not designed to cruise at higher speeds is the potentially adverse interference resulting from the interaction of the airframe and propulsion system flow fields (ref. 17). Also, the details of the nacelle installation may significantly influence the selection of the optimum propulsion system cycle and may alter the design of important components such as the inlets, compressors, and nozzles. It is imperative that the airframe flow field not cause adverse conditions for these components. Therefore, selection of the proper engine nacelle design and how it is integrated with the airframe are important factors that must be understood in attempting to increase cruise speed efficiently.

In order to investigate the integration of the propulsion systems for this type of aircraft, the Lewis Research Center is conducting a series of wind tunnel tests which include both aft-fuselage and underwing engine installations. Both nacelle locations have advantages (refs. 7, 15, and 16), and the resulting configuration may employ a combination of the two. In these tests, both flow-through nacelles and powered nacelles are being used to simulate the proposed high-bypass-ratio turbofan engines (refs. 8 to 14). The present investigation includes the results of the first series of these tests, in which flow-through nacelles were investigated in an aft-fuselage installation.

During this test phase a series of flow-through nacelles were tested with the aft fuselage of an approximately 1/30th-scale model of an advanced CTOL subsonic transport spanning the Lewis 8- by 6-Foot Supersonic Wind Tunnel. Since successful nacelle integration at speeds approaching Mach 1.0 depends on area ruling of the overall configuration to minimize pressure drag (ref. 16), the present nacelles were integrated into the aft fuselage by using local area ruling. Aft-fuselage axial force and pressure data were obtained with nacelles simulating two values of inlet mass flow ratio. Mass flow ratios of 0.6 and 0.46 (based on maximum nacelle cross-sectional area) were tested to simulate a representative full-scale engine value and one which would exist with a powered-turbofan engine simulator, respectively. Two inlet cowl geometries

were investigated. An aft fuselage without nacelles which had an area distribution similar to the configurations with nacelles was tested and used as a reference. By interchanging nacelle-fuselage combinations, several variations in the amount of area ruling were also investigated. Boundary-layer and local flow angularity measurements were made on the reference aft fuselage near the potential nacelle inlet locations. Data were obtained over a Mach number range of 0.6 to 1.0, with an emphasis on the cruise Mach numbers (0.9 to 0.98).

Data were also obtained over a range of angle of attack from 0° to 4.2°, with an emphasis on the projected cruise angle of 3.2° (refs. 7 and 16). The results of these investigations are presented herein.

These tests were performed in the U.S. customary system of units. Conversion to the International System of Units (SI) was done for reporting purposes only.

APPARATUS AND PROCEDURE

Tunnel Installation and Test Conditions

Details of the model installation in the transonic test section of the Lewis 8- by 6-Foot Supersonic Wind Tunnel are shown in figure 1. Schematic drawings of both the side and plan views are shown (figs. 1(a) and (b)), along with a photograph of the model installed in the tunnel (fig. 1(c)). In order to minimize model support effects, especially for aft-fuselage nacelle installation studies, the model was mounted from the wingtips, which, as is discussed in the section Model Details, were modified. Because of the thin wings and large lift loads generated at angle of attack, a thin forward-swept strut had to be added to the lower side of the forward fuselage. The modified wingtips intersected the tunnel wall through trunions which allowed a possible range of model angle of attack of $\pm 5^{\circ}$. The model was located in the upstream portion of the modified 2.44-meter (8-ft) test section, based on the results of a series of calibration model tests (ref. 18). This resulted in the trunion centerline being located 1.74 meters from the end of the perforated test section. Tunnel porosity was maintained at 3.2 percent with local variations near the wingtips as large as 6 percent (fig. 1(c)). This increased local porosity was used to minimize any potential interference associated with the increased wing chord and span (based again on the results reported in ref. 18). Maximum model cross-sectional blockage was slightly under 1 percent at 0° angle of attack which, based on the results of reference 19, would have minimal tunnel blockage effects to nearly Mach 0.98. The present tests were conducted over a range of Mach number from 0.6 to 1.0 at angles of attack from 0° to 4.2°. Reynolds numbers varied from 12.25×10^6 per meter at Mach 0.6 to 15.0×10^6 per meter at Mach 1.0.

Model Details

Schematic drawings of the model details are shown in figure 2. Plan and side views are presented in figures 2(a) and (b), respectively; and cross-sectional cuts through the model are presented in figure 2(c). Forward-fuselage instrumentation details are shown in figure 2(d), and details of the forward-swept support strut are shown in figure 2(e). The configuration shown here incorporated an NASA supercritical wing, an extensively area-ruled fuselage, two aft-fuselage-mounted flow-through nacelles, and a T-tail. The model was constructed such that the aft section from the metric break (X/L = 0.614) to the end of the model was attached through an axial force balance system. (All symbols are defined in appendix A.) Thereby the axial force on the last 40 percent of the model could be measured. The basic model geometry from the nose back to the metric break was scaled up geometrically from the model described in reference 7 except for the wing sections, from semispan station Y = 35.25 centimeters to the tunnel walls. The scale factor was 1.38778 and was determined based on the size of an existing 8.9-centimeter-diameter turbofan engine simulator to be used in future powered-nacelle tests. Since the model here was not sting mounted, the aft fuselage was geometrically different than the model of reference 7. However, the aft fuselage and empennage were designed to conform to the overall area distribution of figure 6. Both the horizontal and vertical tails were geometrically the same as those in reference 7, except for the lower section, which had to be redesigned since an S-duct-type engine nacelle installation was simulated in the vertical tail of reference 7.

This model configuration incorporates a low wing with a root incidence of approximately 2^{o}. The wing, as mentioned previously, was scaled directly out to wing semispan station Y = 35.25 centimeters. In order to be able to support the model with a minimum of support interference and also to provide enough room for the required instrumentation and high-pressure air lines, the wing section was then designed with a constant chord to the tunnel sidewalls. As mentioned previously the results of reference 18, in which a similar wing geometry was tested, indicate that this geometric change to the wing would have little effect on the aft-fuselage flow to Mach 0.975 if the local tunnel sidewall porosity was increased to 6 percent (fig. 1(c)). For this report, however, all aerodynamic coefficients were referenced to the scaled wing area of reference 7, as shown by the dashed wing in figure 2(a). The airfoil coordinates for this wing are given in reference 7.

As described in reference 7 the fuselage back to the metric break was shaped by area-rule concepts refined for second-order effects. The forebody coordinates are listed in table I and are described by the normal cross sections in figure 2(c). The aft fuselage shown in figures 2(a) and (b) incorporates one pair of the four flow-through nacelle designs tested and is also described by the normal cross sections shown in figure 2(c). The aft-fuselage and nacelle details of all the configurations tested are discussed

later in this section. The vertical tail incorporated a symmetrical supercritical airfoil section; its coordinates are presented in reference 7 for most of the geometry except, as mentioned previously, near the forward portion close to the wing root. The horizontal tail was installed at a -1.0° incidence angle, which would be the approximate trim angle for a 3.2° cruise angle of attack. Nondimensional coordinates for this horizontal tail can again be found in reference 7.

The forward-fuselage pressure instrumentation is shown in figure 2(d). Pressure orifices were located on the right half of the model at angular position coordinates φ of 0°, 45°, 90°, and 180°. Instrumentation was also installed in the seal gap on both sides of the metric break and at several locations inside the fuselage to correct the balance for internal pressure forces.

Details of the forward-swept strut are shown in figure 2(e). As mentioned previously the strut was incorporated to minimize the wing deflections at angle of attack. The strut used a symmetrical supercritical airfoil section and was swept forward at approximately 45° (at model angle of attack α of 0°). The strut was pivoted at both ends and allowed the model to move through the desired range of angle of attack. A similar thin-strut configuration was evaluated in the calibration model tests of reference 18 and found to have minimal effects on the aft-fuselage flow field.

The model internal details are shown in figure 3. The overall geometry is shown in figure 3(a) and the metric gap seal details are shown in figure 3(b). The aft fuselage was mounted to the forward fuselage through a flexure-type balance which contained two load cells. The system was designed such that high-pressure heated air (4.83 MN/m^2 at 339 K) could be brought across the balance to power as many as three 8-centimeter-diameter turbofan engine simulators. This was accomplished through a series of matched opposing bellows. Four air lines are shown in figure 3(a); however, the fourth line was used only as an instrumentation duct. An internal scanner-valve data system was attached to the metric portion of the model so that fuselage and nacelle pressures could be measured with a minimum of interference on the force-measuring system. Six valves were installed in two banks of three. In order to prevent internal model cross-flows at the metric break, a soft molded rubber seal was installed between the metric and grounded portions of the model as shown in figure 3(b). As mentioned previously a series of pressure orifices were located inside the gap on both the upstream and downstream sides, which then allowed a correction to be made to the balance. Similar corrections were also made for the internal model pressure forces.

The aft-fuselage configurations tested are shown in figure 4. They included a reference configuration without nacelles and two configurations with side-mounted flow-through nacelles. Each aft fuselage, as is discussed in the section Area Distribution Details, was designed to essentially the same area distribution. The two configurations with flow-through nacelles differed based on the type of nacelle tested. The two nacelles had cylindrical flow-through passages of different internal diameters, which resulted in

two simulated mass flow ratios (based on maximum nacelle diameter) m/m_0 of 0.46 and 0.6. Since these nacelles had different blockage area distributions, an aft fuselage was designed for each. The reference configuration tested is described in figure 4(a) and the flow-through nacelle configurations in figure 4(b).

The reference fuselage was designed to the area distribution of figure 6 with low closure angles to minimize drag and possible flow separation. This resulted in a representative closure for this type of aircraft. It was used to provide a base drag level from which axial force increments could be determined when the nacelles were installed on the other fuselage configurations. The geometric development was based on a series of elliptical sections; the coordinates are listed in the table in figure 4(a-1). A closeup view of the reference aft fuselage installed on the model is shown in figure 4(a-2). The instrumentation, shown in figure 4(a-3), included static orifices, boundary-layer rakes, and conical flow angularity probes. The boundary-layer rakes and angularity probes were tested at one axial location on the fuselage to survey the flow in the general locality where a typical top- or side-mounted engine nacelle would be located. The conical flow angularity probe (fig. 4(a-4)) included a total-pressure probe and four static-pressure orifices located on the conic surface at 90° to one another. They were calibrated in a free-jet facility to yield both flow angle and Mach number in the vertical and horizontal planes. They were located on the model at a distance from the fuselage corresponding approximately to the inlet centerline and were alined such that data in the vertical and horizontal planes would be obtained referenced to free-stream tunnel flow. The reference fuselage with the boundary-layer rakes (fig. 4(a-5)) installed is shown in figure 4(a-6).

Details of the aft-fuselage geometries with the flow-through nacelles are shown in figure 4(b). The coordinates for the two geometries tested are listed in the table in figure 4(b-1). These geometries were again developed from a series of elliptical sections. All cross-sectional area changes to the fuselage were made in the region of the nacelle and were accomplished by changing the elliptical section widths and heights. As mentioned previously a different fuselage geometry was used for each different nacelle design. However, no changes in fuselage geometry were made when inlet cowl geometry was changed. Changes in inlet cowl geometry resulted in only small changes in nacelle cross-sectional area. Closeup views of the installed nacelles are shown in figures 4(b-2) and (b-3). Instrumentation details for the aft fuselages with nacelles are shown in figure 4(b-4). Several axial rows of static-pressure orifices were located on the fuselage, with a concentration near the nacelles.

Details of the nacelle and pylon geometries tested are shown in figure 5. As mentioned previously two types of flow-through engine nacelles were tested which resulted in simulated inlet mass flow ratios m/m_0 of 0.6 and 0.46 (based on maximum nacelle cross-sectional area). These values were based on consideration of the inlet and ex-

panded exit flow properties for typical full-scale engine values and those which would exist with a powered-turbofan engine simulator, respectively. Powered-turbofan engine simulators usually operate at mass flow ratios less than actual engine values since their fan mass flow is deficient by the core flow that would exist for a full-scale engine. The nacelles used herein were designed with constant-area ducts which were sized according to the geometric flow area required for the desired inlet mass flow ratio. A correction was made for the internal-boundary-layer displacement thickness. The inlet for the 0.46-mass-flow-ratio nacelle was longer to obtain a critical Mach number similar to that of the 0.6-mass-flow-ratio inlet, which had a larger internal flow area and highlight area. The displacement thickness was calculated based on flat-plate theory assuming a 1/7th-power profile and resulted in approximately a 1 percent increase in the duct exit diameter. Two inlet cowl geometries were investigated with each simulated mass flow ratio. These included a standard NACA-1 cowl contour and a blunter supercritical cowl contour. The supercritical cowl was a first attempt at designing an inlet cowling based on supercritical airflow concepts. These contours were designed with cowl-length-to-maximum-diameter ratios exceeding 1.2, which, based on the extrapolated results of reference 20 (for the NACA-1 configuration), should result in a design drag-rise Mach number of approximately 0.98 for the range of inlet mass flow ratios and highlight diameters investigated herein. These mass flow ratios corresponded to no appreciable spillage ahead of the nacelle. The nacelle boattails were circular-arc geometries resulting in low boattail angles of 11° and 7.6° for the lower and higher mass flow ratios tested, respectively. The nacelle dimensions and coordinates are given in figures 5(a) and (b).

The nacelles were positioned on the model such that a constant-width or slightly divergent channel resulted between the nacelle and fuselage after both boundary-layer displacement thicknesses were taken into account. This resulted in a 2.9° outboard cant angle. The nacelle instrumentation details are shown in figure 5(c). Five rows of 11 pressure orifices each were located on the external surface of the right nacelle (as the pilot sits). Twelve total-pressure and two static-pressure orifices were located internally on the left nacelle. Details of the nacelle pylons are shown in figure 5(d). The pylons were designed with a low forebody wedge angle to minimize the influence on the channel flow between the nacelle and fuselage.

Area Distribution Details

The area distributions used in the overall model design and the aft fuselages are included in figure 6. In figure 6 the ratio of local cross-sectional area to maximum cross-sectional area A/A_{max} is presented as a function of the ratio of axial distance to over-

all model length X/L'. The overall model-design-envelope area distribution is shown in figure 6(a) and is the same as the one presented in reference 7. This area distribution was derived from tests of bodies of revolution and from theory. The details of the area distributions of the aft fuselages, pylons, and nacelles investigated herein are shown in figure 6(b). The reference aft-fuselage area distribution is shown in figure 6(b-1), and those for fuselages with nacelles are shown in figures 6(b-2) and (b-3). As mentioned previously the aft fuselage of the present model differed from the one described in reference 7 because no sting was required. Consequently, the present model was designed to have a more representative closure geometry and therefore a more representative aft-fuselage area distribution.

The flow-through-nacelle area distributions (fig. 6(b-2) and (b-3)) have the stream-tube cross-sectional area removed. As can be seen in figures 6(b-2) and (b-3) the buildup in area of the nacelle inlets is quite rapid, making it extremely difficult for a one-to-one area ruling in this region. The surface contour of the fuselage would result in severe local turning, which could result in local flow separation. Therefore, in these regions the local contours were kept within reasonable limits, with the result that the area distribution had small perturbations from the reference fuselage distribution. Previous results seen in references 7 and 16 indicated that small perturbations such as these could be tolerated without a significant loss in performance.

Boundary-Layer Transition

Boundary-layer transition strips were located on the model as shown in figure 7. The locations and the grit size used were determined from the techniques and conditions described in references 21 to 23. The grit size used upstream of the metric break was no. 80, and that used on the metric portions of the model was no. 120.

RESULTS AND DISCUSSION

Aft-Fuselage Axial Forces

Aft-fuselage axial force coefficient C_A is presented in figure 8 as a function of free-stream Mach number for both the reference configuration and the configuration with flow-through engine nacelles. As mentioned previously these coefficients are referenced to the unmodified wing planform area shown in figure 2. In figure 8, data are presented from Mach 0.6 to 1.0 at an estimated cruise angle of attack α of 3.2° (ref. 7). Data are presented for the two nacelle mass flow ratios m/m_0 tested and for

the two inlet cowl contours. Calculated skin friction drag for each geometry is also presented. The differences in the calculated skin friction among the various configurations seen in figure 8 were due primarily to the difference in configuration wetted area. The shapes of all the aft-fuselage axial force curves were similar and somewhat different than conventional drag curves. As seen in figure 8 the axial force coefficients generally decreased with increasing Mach number until a minimum was reached, usually near the cruise speeds. Further increases in Mach number resulted in an abrupt drag rise. The values of the minimum aft-fuselage axial forces and the drag-rise Mach numbers varied with the aft-fuselage configuration.

Based on the results presented in references 18 and 19 the present data in figure 8 were considered to be free of tunnel blockage and model support interference effects to Mach 0.975. The results of reference 19 for axisymmetric bodies with area distributions similar to that of the present model indicate that the tunnel blockage effects were minimal to Mach 0.98. Likewise, for winged models similar to the present model, tested in the same facility, the results of reference 18 indicate that the interference effects were small through Mach 0.975.

As seen in figure 8 the lowest axial forces were observed with the reference fuselage, being only about 52 drag counts near Mach 0.95. This was an expected result since the reference configuration had the smallest wetted area. The resulting aft-fuselage drag was only about 17 percent of that projected for the overall aircraft configuration at the cruise angle of attack (ref. 7). Drag-rise Mach number occurred near Mach 0.98, which was close to the range of interference-free data. The axial force levels at the cruise speeds were only about 2 drag counts above the calculated skin friction level, indicating very little pressure drag. Because of this low drag level, especially at the cruise speeds, this configuration was considered to provide a good reference drag level for this investigation.

As would be expected, the aft-fuselage axial force levels were considerably higher with the flow-through nacelle configurations than with the reference configuration. As can be seen in figure 8, when the nacelles with the NACA-1 inlet cowl were installed, the drag levels near the cruise speeds increased to about 72 drag counts. However, this was again very close to the calculated skin friction level, which was higher because of the increased wetted area. These results were similar to those of the reference configuration. Drag-rise Mach number was again at the higher end of the cruise speed range near 0.97. Similar results were seen with this cowl for both mass flow ratios tested.

With the blunt supercritical cowl geometry, the axial force levels at the cruise speeds were considerably higher than the calculated skin friction and correspondingly higher than those measured with the NACA-1 geometries. Likewise the drag-rise Mach numbers were lower than those seen with the thinner NACA-1 cowls. Drag-rise Mach numbers of approximately 0.89 and 0.95 were measured for the nacelle mass flow ratios

of 0.46 and 0.6, respectively. Since all the configurations were area ruled on a one-to-one basis, it was evident that other losses were incurred with the blunt supercritical cowl geometries. As is discussed in detail in the next section, a study of the nacelle and fuselage pressures indicated that lower pressures existing on the supercritical cowl were fed onto the fuselage and resulted in higher drag and lower drag-rise Mach numbers. These results were analogous to those presented in reference 16. Here substantial losses were incurred when high local flow turning was attempted on an aircraft model that incorporated underwing nacelles which were installed with proper area ruling.

Incremental axial force coefficients due to nacelle installations are presented in figure 9 as a function of free-stream Mach number at the cruise angle of attack, $\alpha = 3.2^{\circ}$. The axial force increment ΔC_A is defined as the difference in aft-fuselage axial force between the configurations with flow-through nacelles and the reference configuration. Similar increments for the calculated skin friction are also presented. As seen previously in figure 8 the calculated skin friction drags of the nacelle configurations were higher than those calculated for the reference configuration. As mentioned previously, this was due primarily to the increase in wetted area of the nacelle configurations. The results seen in figure 9 indicate that for the blunt supercritical cowls the increments are higher than the corresponding skin friction increments. In the case of the simulated inlet mass flow ratio $m/m_0 = 0.46$, the early drag-rise Mach number is also clearly reflected. These results indicate an unfavorable interference effect which results in increased pressure drag. However, the increments seen in figure 9 for the NACA-1 inlet cowl configurations are close to or below the friction increments especially in the cruise speed range of Mach 0.9 to 0.98. Even after the drag rise, as indicated in figure 8, the increments seen here are nearly the same as the increment in skin friction drag. However, this may be the result of tunnel blockage interference. The results seen from free-stream Mach numbers of approximately 0.8 to 0.975 indicated that favorable interference resulted with the NACA-1 inlet cowl whereby the isolated nacelle pressure drag was more than canceled out when the nacelles were installed. These results also agree with those presented in reference 7 and other unpublished results of work performed at the NASA Langley Research Center by Stuart G. Flechner, where drag levels near skin friction values were measured when aft-fuselage flow-through engine nacelles were installed. Therefore, it can be concluded that flow-through nacelles can be successfully integrated into the aft fuselage of an aircraft configuration designed to cruise at speeds from Mach 0.9 to 0.98 if adverse local geometries are avoided.

In an attempt to better understand the local-area-ruling concepts, a series of tests were made with both under- and over-area-ruled model configurations. The lower-mass-flow-ratio nacelles with the NACA-1 inlet cowl were tested with the aft fuselage designed for the higher-mass-flow-ratio nacelles (under-area-ruled case). The inverse situation (over-area-ruled case) was also tested. These tests resulted in configurations which were 28 percent under area ruled and 37 percent over area ruled, respectively.

The results of these tests are shown in figure 10 and are compared to those of the 100-percent-area-ruled configuration. As seen in figure 10 the results of both over and under area ruling were to increase aft-fuselage axial force at the cruise speeds and to lower drag-rise Mach number. The drag increases seen here resulting from improper area ruling, however, were still generally less than the higher drag levels seen with the blunter supercritical inlet cowls (fig. 9).

The effects of the internal total-pressure rakes installed in the left nacelle duct on aft-fuselage axial force are seen in figure 11. The supercritical inlet cowl geometry nacelles with the simulated mass flow ratio $m/m_0 = 0.46$ were tested both with and without the internal rakes. As seen in figure 11 the rakes resulted generally in less than a 1-drag-count increase. Therefore, it was decided not to remove the rakes during the testing.

Also during the testing it was noted that, on certain days with higher humidity conditions, condensation was occurring in the flow off the horizontal tail at Mach 1.0 when the tunnel dryer beds were not used. Based on the results of reference 24 it was feared that the humidity level might be influencing the drag especially at the cruise speeds and above. Therefore, the model was tested both with and without the dryer beds in the tunnel circuit, and the results are shown in figure 12. As seen in figure 12 the effects of humidity were negligible. The absolute humidity level produced by the beds was not measured, but when the beds were used there was no condensation in the flow off the tail. Therefore, it was concluded that the effects of humidity on this series of tests were negligible.

The effects of increasing angle of attack on aft-fuselage axial force are shown in figure 13, both with and without flow-through nacelles. Only the NACA-1 inlet cowl nacelles with the simulated mass flow ratio $m/m_0 = 0.6$ were tested over the complete range of angle of attack from 0° to 4.2°. As seen in figure 13 the effects were similar for both types of aft fuselage tested. The effects of increasing angle of attack were generally to reduce aft-fuselage axial force. The force level at the highest angle of attack was less than the calculated friction drag. Increasing angle of attack also resulted in an increase in drag-rise Mach number to a maximum of 0.97 (0.98 with the reference fuselage) at the cruise angle of attack $\alpha = 3.2^\circ$. At higher angles the drag-rise Mach number decreased slightly.

Fuselage and Nacelle Pressures

A comparison of the fuselage pressure distributions with the different inlet cowl contours tested is shown in figure 14. Local pressure coefficient C_p is presented for the two inlet cowl contours with simulated inlet mass flow ratio $m/m_0 = 0.6$. This mass flow ratio corresponds to little or no spillage around the cowl lip. Data are pre-

sented as a function of fuselage nondimensional position coordinate X/L for three cruise Mach numbers - 0.92, 0.95, and 0.97. These results are typical for all the cases where large differences in aft-fuselage axial force were observed (fig. 8). As can be seen in figure 14 the pressure distributions along the fuselage are complex, with several regions of flow expansion and recompression. The most significant differences in pressure distribution among the various configurations were in the region just aft and under the leading edge of the nacelles (X/L = 0.7). A region of much lower pressure is seen on the fuselage at this location with the supercritical cowl geometry than with the NACA-1 inlet cowl geometry. As can be seen from the model sketch in figure 14, this region of lower pressure is located directly on the aft-facing region of the area-ruled fuselage and is consequently contributing to the increased axial force level. This region of low pressure becomes more severe with increasing Mach number. And as can be seen in figure 14, when compared to the $C_{p,\,sonic}$ level, this local flow is evidently supersonic. This region is then followed by an abrupt pressure rise or recompression, especially in the channel between the nacelle and fuselage, which is evidently a strong normal shock. This shock may adversely affect the boundary layer in this region and result therefore in a further increase in aft-fuselage axial force and a decrease in performance. These trends do not exist with the NACA-1 inlet cowl configuration.

Nacelle pressures on the two types of inlet cowl contours are presented in figure 15. Data are presented for the supercritical cowl contour with both simulated inlet mass flow ratios and are compared to the NACA-1 cowl contour pressures measured for the simulated mass flow ratio $m/m_0 = 0.6$. Data are again compared at free-stream Mach numbers of 0.92, 0.95, and 0.97 at the cruise angle of attack, $\alpha = 3.2^{\circ}$. It can be seen in figure 15 that the most notable differences in the nacelle pressures exist on the inlet cowls. The pressures on the blunt supercritical cowl are much lower than those on the NACA-1 contour. The lowest cowl pressures are seen with the simulated inlet mass flow ratio $m/m_0 = 0.46$. This configuration had the correspondingly highest value of aft-fuselage axial force coefficient. These low pressures feed over to the fuselage just aft of the nacelle leading edge and result in low fuselage pressures and higher axial force, as shown in figures 14 and 8, respectively. It is evident that the cowl suction forces resulting from these lower pressures did not compensate for the increased fuselage axial force. Also, as shown in figure 15, when the low pressures on the cowl are compared to the $C_{p,\,sonic}$ level, it is evident that this flow is supersonic. Similar to the results on the fuselage (fig. 14), this supersonic flow may be recompressing through a strong normal shock ($x/l \sim 0.15$). This recompression is not seen with the NACA-1 inlet contour. These results combined with the results in figure 10 indicate that the pressure field created by the supercritical cowl geometry was responsible for the decreased aft-fuselage performance. It must be noted, however, that the adverse effects associated with the blunt supercritical cowl might possibly be mitigated if the inlet flow

spillage ahead of the cowl leading edge were properly simulated. The flow-through nacelles that were tested herein did not spill an appreciable amount of flow ahead of the cowl lip as an actual engine installation would. This will be investigated in an upcoming series of tests where this model will be tested with powered-engine simulators.

The effects of the nacelles on the forward-fuselage pressures are shown in figure 16. Data are compared between the reference configuration and the NACA-1 inlet contour nacelle configuration at the simulated inlet mass flow ratio $m/m_0 = 0.6$. The comparisons are shown at the representative Mach numbers - 0.92, 0.95, and 0.97 - at the cruise angle of attack. As shown in figure 16 the nacelles had a negligible effect on the forward-fuselage pressures. These same results were seen with the other nacelle geometries at all the Mach numbers tested.

More detailed fuselage and nacelle pressure distributions for an expanded range of Mach number and angle of attack are included in appendix B.

Nacelle Total-Pressure Recovery and Mass Flow Ratio

The effects of nacelle geometry and model angle of attack on the nacelle-duct, average, total-pressure recovery $\bar{P}_T/P_{T_0}$ are shown in figure 17. The average total-pressure recovery in the nacelle duct was 0.998 for all the configurations, Mach numbers, and angles of attack tested. However, it must be noted again that the internal rakes used did not survey the boundary-layer profile close to the duct walls and that the internal geometry was cylindrical, so that the total pressures presented are not a true inlet recovery.

The effects of nacelle geometry and model angle of attack on nacelle calculated mass flow ratio m/m_0 are shown in figure 18. The nacelle mass flow ratio was calculated based on the maximum nacelle cross-sectional area and the internal nacelle pressure. The average total pressure was combined with the static pressure measured near the end of the nacelle duct. Since the duct boundary layer was not measured, the geometric duct area was corrected based on a flat-plate, 1/7th-power calculation of the displacement thickness. As shown in figure 17 the calculated mass flow ratios for all conditions were within 96 percent of the design value and did not vary significantly with Mach number or angle of attack.

Reference Aft-Fuselage Boundary-Layer and Flow Angularity Characteristics

Boundary-layer characteristics measured on the reference aft fuselage are presented in figures 19 and 20. As mentioned previously, boundary-layer measurements

were made on the reference aft fuselage at the axial locations where possible nacelle inlets would be located. Three angular coordinate positions φ were surveyed - 0° (top), 270° (side), and 295° (side above model centerline). The top axial location (0°) was at nondimensional position coordinate $X/L = 0.67$, and the side axial location (270°) was at $X/L = 0.69$. Boundary-layer velocity profiles for each rake are shown in figure 19, and these values were integrated by using the trapezoidal rule to yield the displacement thickness and the momentum thickness. The probe-measured velocities were referenced to the maximum local velocity, assuming a constant static pressure through the boundary layer. A flat-plate, 1/7th-power calculation of the boundary-layer thickness δ_{fp} was made for each Mach number and is shown in the figure. In general, these profiles indicate that the local flow was not adversely disturbed by the upstream model geometry. Only a small variation was evident from the side to the top of the fuselage. The profiles also indicate that the boundary-layer depths were close to flat-plate theory. In addition, the depths of the boundary layer were such that the design fuselage separation distances selected for the inlets (fig. 2(c)) were adequate to avoid any boundary-layer ingestion. Typical reference-aft-fuselage, boundary-layer velocity profiles are shown in figure 20, referenced to the boundary-layer thicknesses which were estimated from figure 19. Data are shown at a free-stream Mach number of 0.97 at the cruise angle of attack and are compared to a theoretical, 1/7th-power, flat-plate profile. As shown in figure 20 the profiles measured on the aft fuselage are of a power somewhat higher than 1/7.

Local flow angles measured at the same axial locations and angular coordinate positions as the boundary-layer values are presented in figure 21 as a function of free-stream Mach number at the cruise angle of attack. These data were obtained by using calibrated conical flow angularity probes which were mounted on the reference fuselage at distances from the fuselage corresponding to the nacelle inlet centerline standoff distance. The probes were calibrated to yield both flow angle and local Mach number in two planes parallel to the model axis - a vertical (or upwash) plane and a horizontal (or sidewash) plane. As mentioned previously the probe tips were alined parallel to the model centerline with the orifices alined to measure upwash and sidewash angles (fig. 4(a-3)). As shown in figure 21 the probe on top of the fuselage ($\varphi = 0^{\circ}$) showed a 1° to 2° upwash angle and a near-zero sidewash angle over the Mach number range tested. The probe on the side of the fuselage ($\varphi = 270^{\circ}$) indicated only a small upwash angle of generally less than 0.5° and a sidewash angle of from 2.2° to 3.2°. The positive outwash angle at this location is probably due to the local fuselage geometry. A plan view of this region (fig. 4(a-1)) shows that the local body contour in the region of the probe is turning outboard at about the same angle. The data observed at the side location above the model centerline ($\varphi = 295^{\circ}$) indicate both upwash and sidewash angles of from 2.5° to 3.9°. The flow-through nacelles used in this test were canted outboard at 2.9°

(fig. 2(a)), so the local flow may have been as high as 6° to the inlet face. Therefore, some benefit might be possible if the inlet were canted to be more closely alined with the local flow, particularly for the case where significant spillage ahead of the inlet lip is present. However, this in turn would result in a further complication of the local-area-ruling problem.

Local Mach numbers measured with the conical angularity probes are shown in figure 22. Data are presented as a function of free-stream Mach number with the model again at the cruise angle of attack. At free-stream Mach numbers of generally 0.85 and below the measured Mach numbers were close to or above free-stream values. However, at cruise speeds above Mach 0.9 the measured Mach numbers were slightly suppressed. These results are significant in regard to the basic inlet design. As was mentioned previously the nacelle inlets were designed for a drag-rise Mach number of approximately 0.98. Therefore, these results suggest that a lower design drag divergence Mach number could have been selected which could have resulted in a shorter length of the external cowl. Based on the data in figure 22, favorable results might have been possible with a design drag divergence Mach number as low as 0.94 for the side-mounted nacelles and approximately 0.95 for a top-mounted nacelle. For the side-mounted nacelles of this investigation, this could have resulted in approximately a 30 percent reduction in the external length of the cowl contour, based on an extrapolation of the design charts of reference 20.

SUMMARY OF RESULTS

In order to investigate the problems associated with the integration of aft-fuselage engine nacelles on a CTOL transport-type aircraft designed to cruise between Mach 0.9 and 0.98, a series of tests were conducted in the Lewis 8- by 6-Foot Supersonic Wind Tunnel. An approximately 1/30th-scale, full-span model was tested with flow-through nacelles to determine aft-fuselage axial force and pressure distributions for a series of locally area-ruled aft fuselages designed for nacelle installation. Two nacelles with different cylindrical flow-through diameters which simulated inlet mass flow ratios of 0.46 and 0.6 were investigated. An NACA-1 inlet cowl and a blunter supercritical cowl were also investigated. Several variations in the amount of local area ruling were investigated. An aft fuselage without nacelles but with a similar area distribution was tested for reference. Boundary-layer and local flow angle measurements were made near the nacelle inlet locations. Data were obtained over a Mach number range from 0.6 to 1.0, and angle of attack was varied from 0° to 4.2°. The following observations were made:

1. With the reference fuselage a high drag-rise Mach number of nearly 0.98 was observed at the cruise angle of attack (3.2°). The axial force levels seen near the cruise speeds (Mach 0.9 to 0.98) and angle of attack were only 17 percent of those pro-

jected for the complete aircraft and were only about 2 drag counts higher than the calculated skin friction.

2. With aft-fuselage-mounted, flow-through engine nacelles the axial force levels were higher, as would be expected. However, the incremental increases seen with the thinnest nacelle cowl geometry (NACA-1) were less than the calculated incremental increase in skin friction at Mach numbers from approximately 0.8 to 0.975 for the cruise angle of attack. These results indicate that a favorable interference effect more than canceled out the nacelle pressure drag. Drag rise was observed to occur near Mach 0.97. Consequently, these flow-through-nacelle results indicate that efficient cruise may be obtained on this type of aircraft with aft-fuselage-mounted engine nacelles in the speed range from Mach 0.9 to nearly 0.98.

3. With full-flowing (no spillage at inlet lips) flow-through nacelles, an unfavorable inlet cowl geometry can have deleterious effects on both axial force level and drag-rise Mach number. With a thickened cowl shape (supercritical), lower pressures were observed on the cowl than with a thinner geometry (NACA-1). These low pressures fed onto the aft-facing region of the locally area-ruled fuselage and resulted in a significant increase in axial force and a decrease in drag-rise Mach number to 0.89 (for the 0.46-mass-flow-ratio configuration).

4. With the NACA-1 inlet cowl nacelles properly area ruled into the fuselages, the effects on axial force and drag-rise Mach number of simulating two different inlet mass flow ratios, by using two different nacelles and fuselages, were negligible. The results observed for both over- and under-area-ruled configurations were generally an increase in axial force and a decrease in drag-rise Mach number.

5. The effects of the flow-through nacelles on forward-fuselage pressures were negligible.

6. The effect of increasing angle of attack was to reduce aft-fuselage axial force both with and without nacelles. Increasing angle also resulted in increased drag-rise Mach number to a maximum at the cruise angle of attack (3.2°). At higher angles of attack the drag-rise Mach number decreased.

7. Fuselage boundary-layer thicknesses measured on the reference fuselage at the axial stations where the nacelle inlets were located were of similar order as flat-plate calculations; and the profiles were undisturbed by the upstream airframe flow field. Therefore, the design model inlet centerline displacements from the fuselage were adequate to avoid boundary-layer ingestion.

8. Local flow angles measured on the reference aft fuselage near the axial location of the flow-through-nacelle inlets were generally low, with a maximum of 3.9° being observed for a side-mounted nacelle located above the model centerline. Since the nacelles in this investigation were canted outboard, these results indicate that some benefit may be obtained with inlet cant. However, this would complicate the local-area-ruling problem.

9. The local Mach numbers observed on the reference aft fuselage near the nacelle inlet locations were slightly suppressed near the cruise speeds and unaffected at the lower speeds. Since the nacelle inlet cowls were designed for a drag-rise Mach number of 0.98, these results suggest that a lower design drag-rise Mach number could have been used, resulting in shorter external cowls. Favorable results might have been possible with design drag-rise Mach numbers as low as 0.94 for side-mounted nacelles and approximately 0.95 for top-mounted nacelles.

Lewis Research Center,
National Aeronautics and Space Administration,
Cleveland, Ohio, September 13, 1974,
501-24.

APPENDIX A

SYMBOLS

A	model cross-sectional area
A_{max}	maximum design-envelope model cross-sectional area, 392.67 cm^2
a	spanwise fuselage ellipse semiaxis, cm
b	vertical fuselage ellipse semiaxis, cm
b/2	wing semispan of reference planform (fig. 2(a)), 75.79 cm
C_A	aft-fuselage axial force coefficient, (Axial force)/$S_w q_0$
ΔC_A	increment in axial force coefficient between configuration with nacelles and reference fuselage, Δ(Axial force)/$S_w q_0$
C_p	pressure coefficient, $(p - p_0)/q_0$
$C_{p,sonic}$	pressure coefficient corresponding to M = 1.0 local flow
c	wing or support strut chord, cm
c_{ht}	horizontal tail chord, cm
c_{vt}	vertical tail chord, cm
c_w	wing chord at tunnel wall, 24.43 cm
d_{inlet}	nacelle internal diameter, cm
d_{max}	nacelle maximum diameter, 8.001 cm
h	height of boundary-layer rakes, 2.66 cm
L	fuselage length, 200.914 cm
L'	overall model length, 214.78 cm
l	nacelle length, cm
l_s	nacelle strut reference length, cm
M	measured local Mach number
M_0	free-stream Mach number
m	calculated nacelle captured mass flow, kg/sec
m_0	maximum nacelle mass flow based on nacelle maximum diameter and free-stream conditions, kg/sec

$\bar{P}_T$ average internal nacelle stagnation pressure, N/m^2

P_{T_0} free-stream stagnation pressure, N/m^2

p local static pressure, N/m^2

p_0 free-stream static pressure, N/m^2

q_0 free-stream dynamic pressure, N/m^2

R nacelle radial coordinate

r radius of nacelle boattail contour

S_w wing reference area based on unmodified wing planform (fig. 2(a)), 0.3621 m^2

t thickness coordinate, cm

V local velocity at boundary-layer-rake probe locations, m/sec

V_l local stream velocity at boundary-layer rake, m/sec

X fuselage axial distance coordinate, cm

x support strut or nacelle axial distance coordinate, cm

x_s strut axial distance coordinate, cm

Y model spanwise distance coordinate, cm

y distance from fuselage of boundary-layer-rake probe tips, cm

Z fuselage vertical distance coordinate, cm

ΔZ displacement of fuselage ellipse centerline from model reference line, cm

Z_{sl} strut lower surface coordinate, cm

Z_{su} strut upper surface coordinate, cm

α model angle of attack, deg

δ boundary-layer thickness, cm

δ^* calculated boundary-layer displacement thickness, cm

δ^{**} calculated boundary-layer momentum thickness, cm

φ angular position coordinate, deg

Subscript:

fp flat plate

max maximum

APPENDIX B

FUSELAGE AND NACELLE PRESSURE DISTRIBUTIONS

Reference Fuselage Pressures

Fuselage pressure distributions with the reference aft fuselage are presented in figures 23 and 24. In figure 23, data are presented for the complete Mach number range tested from 0.6 to 1.0 at model angle of attack $\alpha = 3.2^{\circ}$. The distributions over the model are characterized by several expansions and recompressions. The effect of model angle of attack on the reference configuration pressure is shown in figure 24 at a free-stream Mach number of 0.97. Data are presented over a range of angle of attack α from 0° to 4.2°. The most notable effects of increasing angle are seen over the forward fuselage, where the pressures on the bottom increase and those on top decrease. The pressures over the aft fuselage tend to generally increase with increasing angle, especially the low pressures near the nondimensional position coordinate $X/L = 0.8$. This result correlated with the corresponding decrease in axial force with increasing angle of attack shown in figure 13. Similar results were seen at the other Mach numbers tested.

Fuselage Pressures with Flow-Through Nacelles

Detailed pressure distributions on the fuselage for the model configuration which utilized the flow-through nacelles with simulated mass flow ratio $m/m_0 = 0.6$ and with the NACA-1 inlet cowl contour are shown in figures 25 and 26. Data are again presented over the complete Mach number range tested in figure 25 and over the angle-of-attack range in figure 26 at a free-stream Mach number of 0.97. Detailed data are presented with this particular configuration because it is more representative of a typical full-scale configuration and because it yielded the most favorable aft-fuselage performance (with nacelles). The results seen in figures 25 and 26 are similar to those obtained with the reference fuselage.

Nacelle Pressures

Detailed nacelle pressure distributions are shown infigures 27 to 29. The pressure distributions over the complete Mach number range tested for the 0.6-simulated-mass flow-ratio nacelles with the NACA-1 inlet contour are presented in figure 27 at model angle of attack $\alpha = 3.2^{\circ}$. The effects of angle of attack for the same configuration at a free-stream Mach number of 0.97 are shown in figure 28. And pressure distributions for the complete Mach number range tested with the 0.46-simulated-mass-flow-ratio nacelles with the supercritical inlet contour are shown in figure 29.

REFERENCES

1. Study of the Application of Advanced Technologies to Long-Range Transport Aircraft. Volume 1: Technology Applications. General Dynamics Corp. (NASA CR-112090), 1972.

2. Study of the Application of Advanced Technologies to Long-Range Transport Aircraft. Volume 2: Research and Development Requirements. General Dynamics Corp. (NASA CR-112091), 1972.

3. Study of the Application of Advanced Technologies to Long-Range Transport Aircraft. Volume 1: Advanced Transport Technology Final Results. Boeing Co. (NASA CR-112092), 1972.

4. Study of the Application of Advanced Technologies to Long-Range Transport Aircraft. Volume 2: Advanced Technology Program Recommendations. Boeing Co. (NASA CR-112093), 1972.

5. Lange, R. H.; Sturgeon, R. F.; Adams, W. E.; Bradley, E. S.; Cahill, J. F.; Eudaily, R. R.; Hancock, J. P.; and Moore, J. W.: Study of the Application of Advanced Technologies to Long-Range Transport Aircraft. Volume 1: Analysis and Design. Lockheed-Georgia Co. (NASA CR-112088), 1972.

6. Lange, R. H.; Sturgeon, R. F.; Adams, W. E.; Bradley, E. S.; Cahill, J. F.; Eudaily, R. R.; Hancock, J. P.; and Moore, J. W.: Study of the Application of Advanced Technologies to Long-Range Transport Aircraft. Volume 2: Research and Development Requirements. Lockheed-Georgia Co. (NASA CR-112089), 1972.

7. Langhans, Richard A.; and Flechner, Stuart G.: Wind Tunnel Investigation at Mach Numbers from 0.25 to 1.01 of a Transport Configuration Designed to Cruise at Near-Sonic Speeds. NASA TM X-2622, 1972.

8. Beheim, Milton A.; Antl, Robert J.; and Pavolny, John H.: Advanced Subsonic Transport Technology Assessment; Advanced Propulsion: Cleaner and Quieter. Astronaut. Aeronaut., vol. 10, no. 8, Aug. 1972, pp. 37-43.

9. Whitlow, John B., Jr.; Kraft, Gerald A.; and Civinskas, Kestutis C.: Parametric Engine Study for a Mach 0.98 Commercial Air Transport. NASA TM X-52961, 1971.

10. Kraft, Gerald A.; and Whitlow, John B., Jr.: Optimization of Engines for a Mach 0.98 Transport with Low Takeoff and Approach Noise Levels. NASA TM X-67865, 1971.

11. Propulsion System Studies for an Advanced High Subsonic, Long Range Jet Commercial Transport Aircraft. R72-AEG-296, General Electric Co. (NASA CR-121016), 1972.

12. Brines, Gerald L.: Studies for Determining the Optimum Propulsion System Characteristics for Use in a Long Range Transport Aircraft. PWA-4449, Pratt & Whitney Aircraft (NASA CR-120950), 1972.

13. Schwartz, M. B.: Propulsion System Requirements for Advanced Technology Air Transports. Paper 710761, SAE, Sept. 1971.

14. Sussman, M. B.; Gunmarson, D. W.; and Edwards, P.: Nacelle Design Studies for Advanced Transport Aircraft. Paper 72-1204, AIAA, Nov.-Dec., 1972.

15. Goodmanson, Lloyd T.; and Schultz, William H.: Installation and Integration of Transonic Transport Propulsion Systems. Paper 710762, SAE, Sept. 1971.

16. McKinney, Linwood W.; Herman, Joseph F.; and Bodin, Lawrence A.: Effect of Wing Mounted Nacelles on a 42 Degree Swept Supercritical Wing Configuration at Near Sonic Speeds. NASA TM X-2954, 1974.

17. Kutney, J. T.; and Piszkis, S. J.: Reduction of Drag Rise on the Convair 990. Paper 63-276, AIAA, Dec. 1963.

18. Blaha, Bernard J.: Wind Tunnel Blockage and Support Interference Effects on Winged Body Models at Mach Numbers from 0.6 to 1.0. NASA TM X-3011, 1974.

19. Couch, Lana M.; and Brooks, Cuyler W., Jr.: Effect of Blockage Ratio on Drag and Pressure Distributions for Bodies of Revolution at Transonic Speeds. NASA TN D-7331, 1973.

20. Hancock, J. P.; and Hinson, B. L.: Inlet Development for the L-500. Paper 69-448, AIAA, June 1969.

21. Loving, Donald L.: Wind-Tunnel - Flight Correlation of Shock-Induced Separated Flow. NASA TN D-3580, 1966.

22. Blackwell, James A., Jr.: Preliminary Study of Effects of Reynolds Number and Boundary-Layer Transition Location on Shock-Induced Separation. NASA TN D-5003, 1969.

23. Braslow, Albert L.; and Knox, Eugene C.: Simplified Method for Determination of Critical Height of Distributed Roughness Particles for Boundary Layers Transition at Mach Numbers from 0 to 5.0. NACA TN 4363, 1958.

24. Jordon, Frank L., Jr.: Investigation at Near Sonic Speed of Some Effects of Humidity on the Longitudinal Aerodynamics Characteristics of a NASA Supercritical Wing Research Airplane Model. NASA TM X-2618, 1972.

TABLE I. - FORWARD-FUSELAGE RADII

[Center of radii, 0.634 cm below reference centerline.]

Upper and lower fuselage		Upper fuselage only	
Nondimensional position coordinate, X/L	Radius, cm	Nondimensional position coordinate, X/L	Radius, cm
0	0	0.439	8.707
.018	3.843	.456	8.318
.035	5.076	.474	8.002
.053	5.958	.491	7.720
.070	6.663	.509	7.544
.088	7.261	.526	7.473
.105	7.755	.544	7.508
.123	8.178	.561	7.613
.140	8.565	.579	7.790
.158	8.918	.597	8.037
.175	9.236	[a].614	7.905
.193	9.517		
.211	9.764		
.228	9.975		
.246	10.152		
.263	10.293		
.281	10.364		
.298	10.364		
.316	10.328		
.333	10.257		
.350	10.152		
.368	9.975		
.386	9.764		
.404	9.483		
.421	9.130		

[a]Metric break.

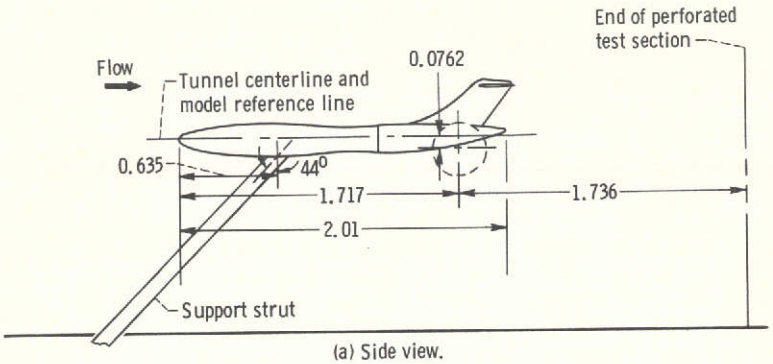

(a) Side view.

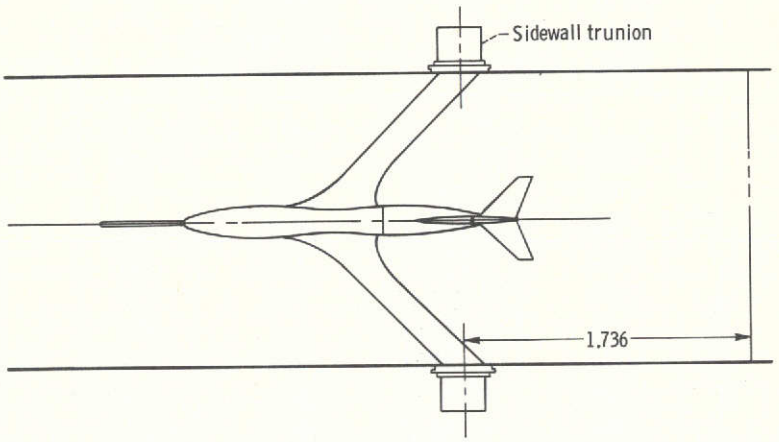

(b) Plan view.

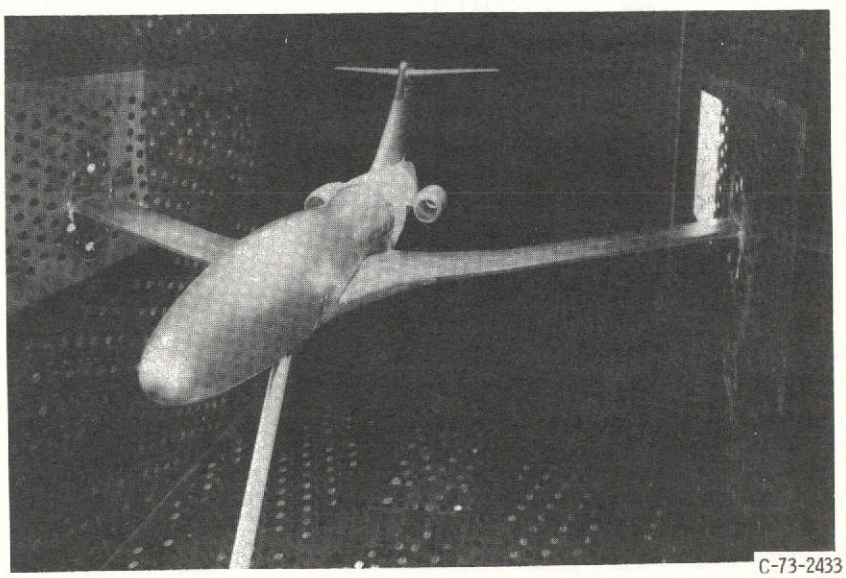

(c) Model in tunnel.

Figure 1. - Model installation in transonic test section of 8- by 6-Foot Supersonic Wind Tunnel. (Dimensions are in meters.)

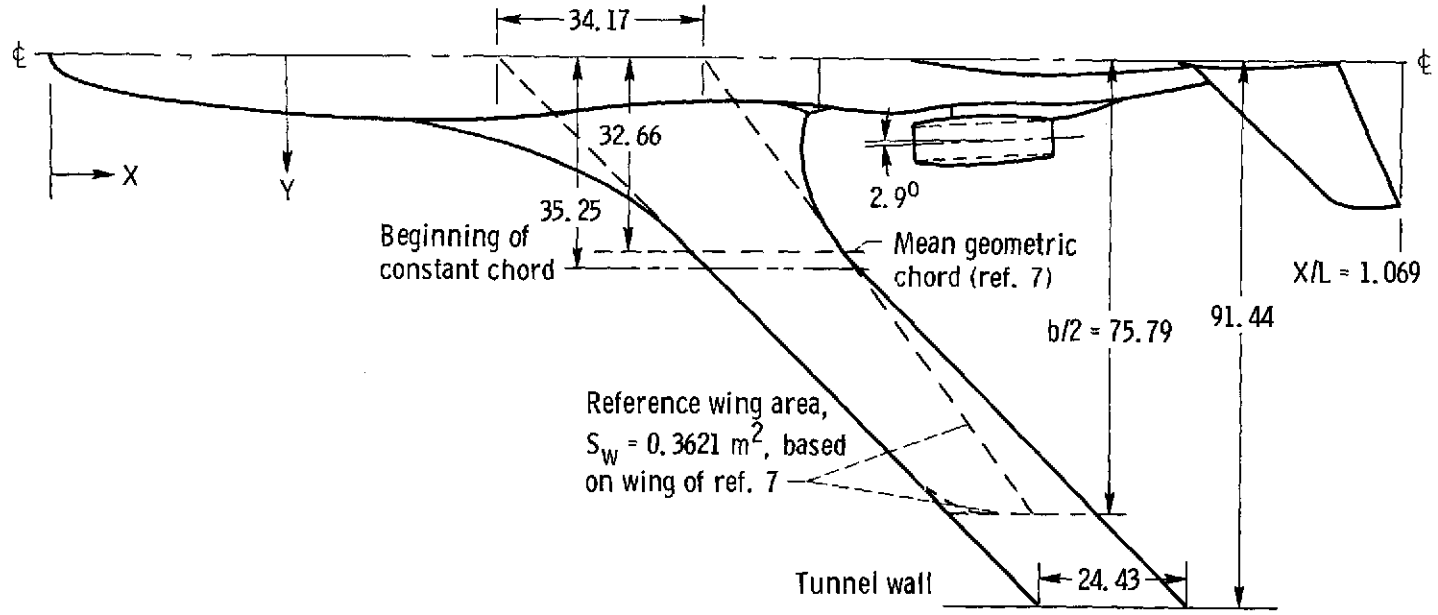

(a) Plan view.

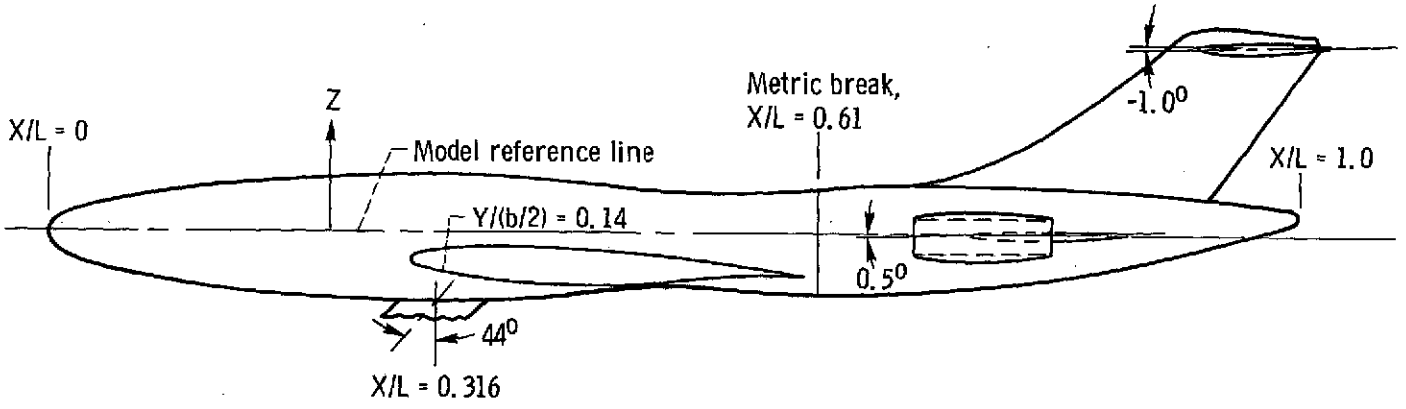

(b) Side view.

Figure 2. - Model description. Nacelles with simulated mass flow ratio, m/m_0 = 0.6; fuselage length, L = 200.914 centimeters. (Dimensions are in centimeters.)

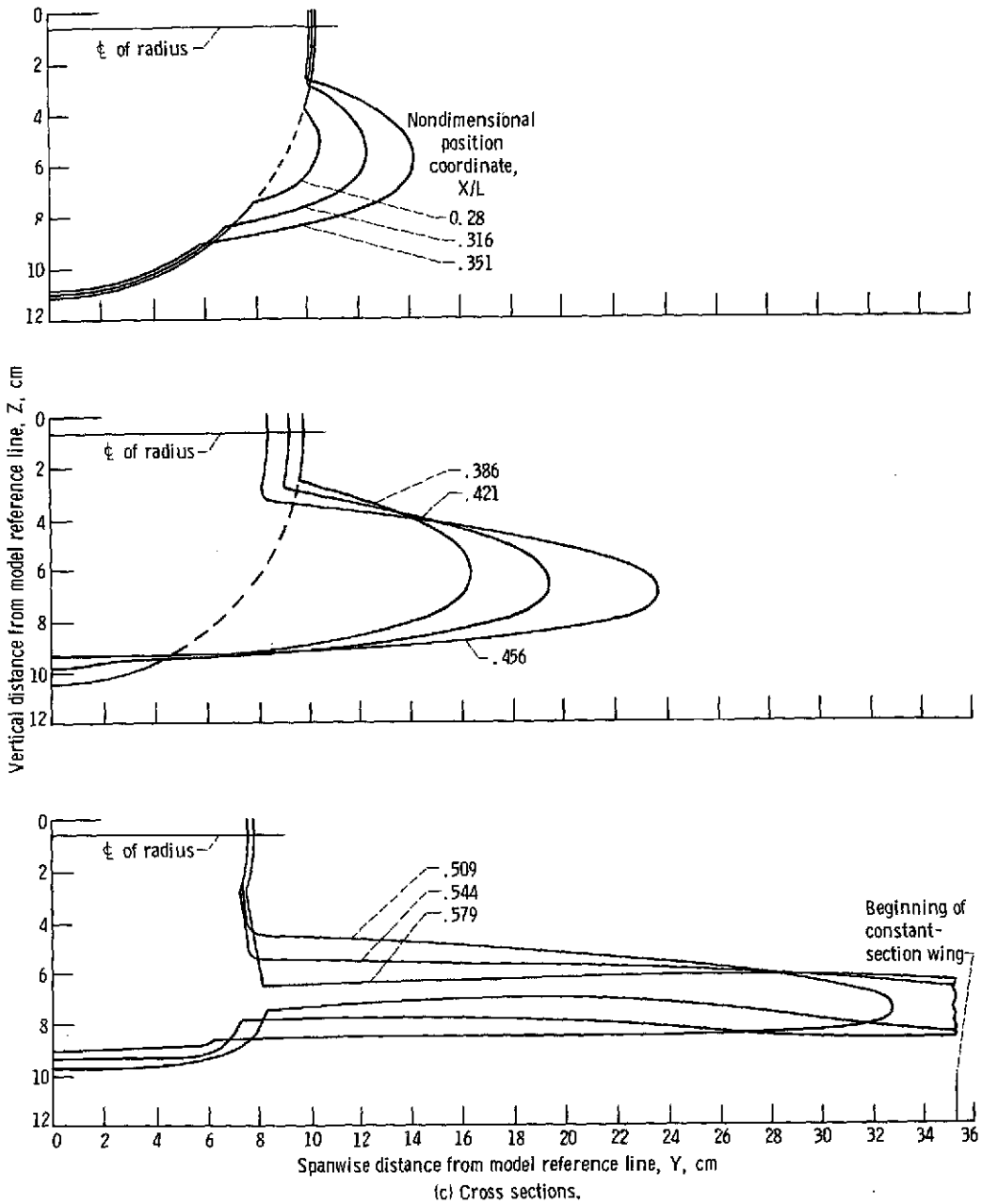

(c) Cross sections.

Figure 2. - Continued.

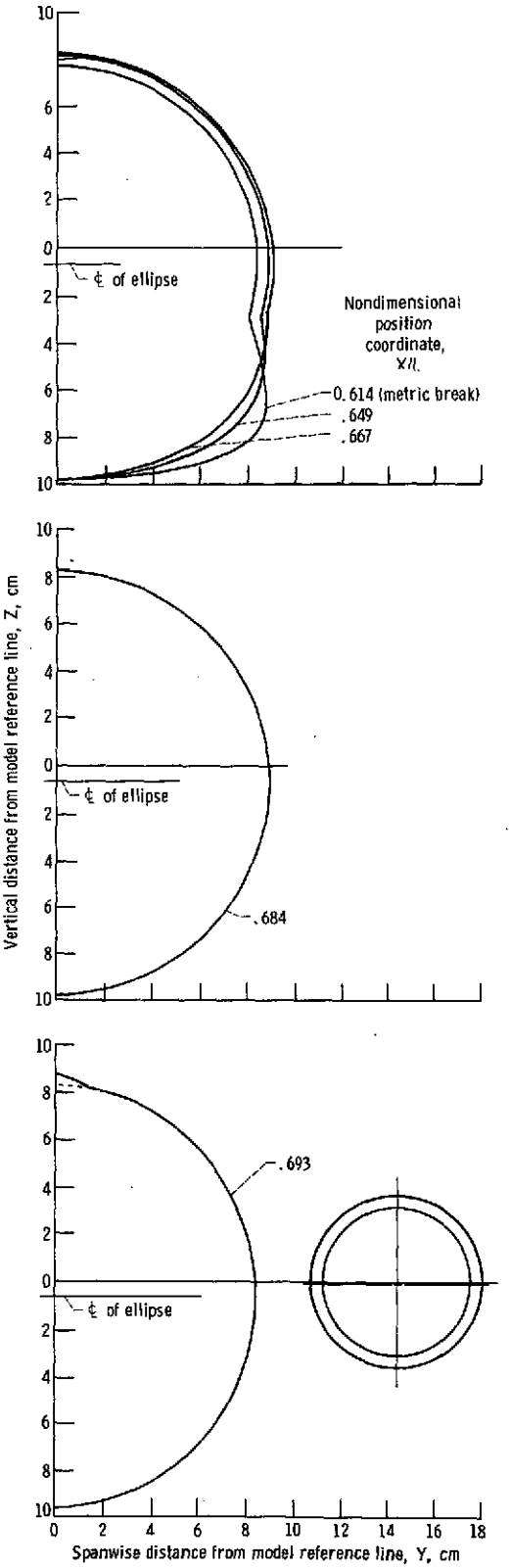

(c) Continued.

Figure 2. - Continued.

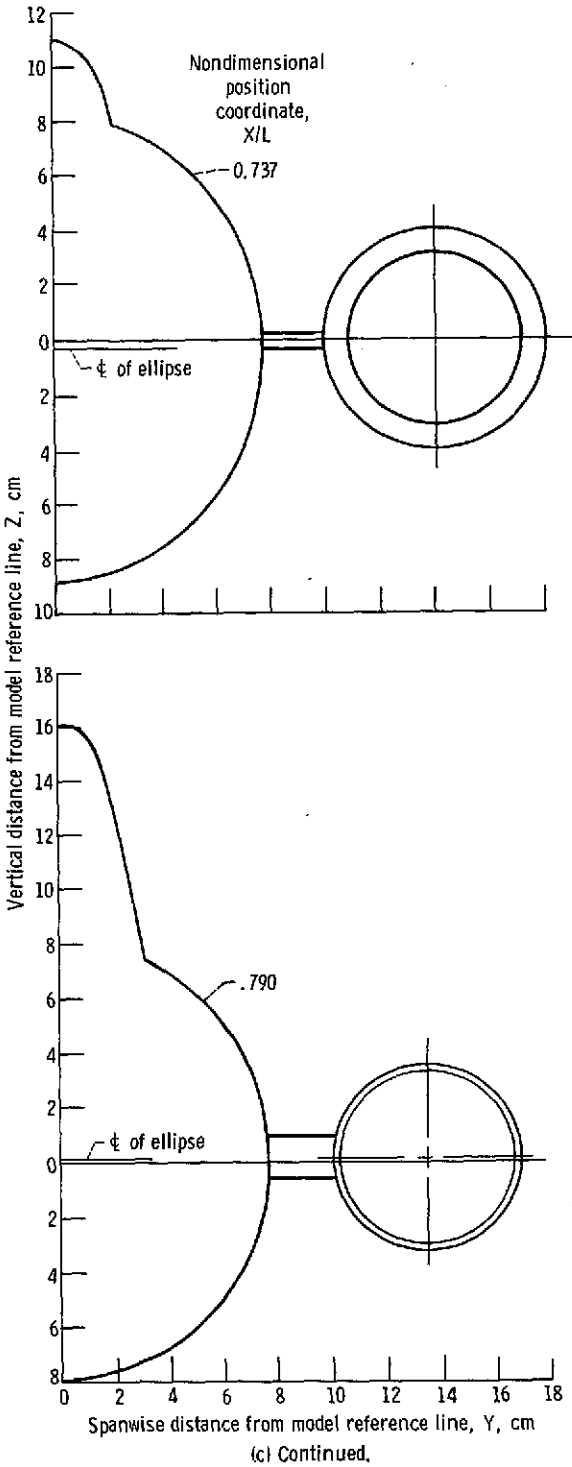

(c) Continued.

Figure 2. - Continued.

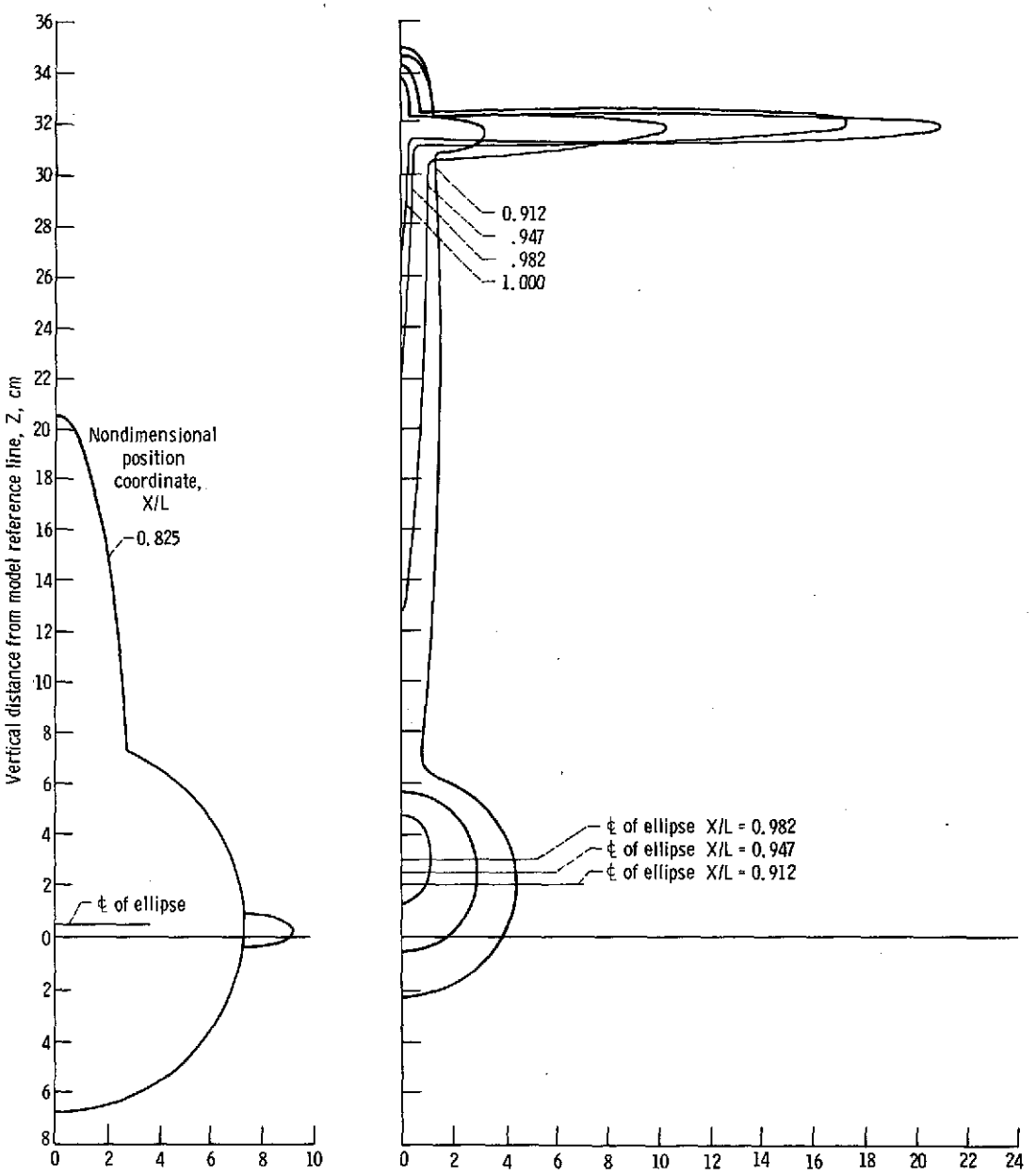

(c) Concluded.

Figure 2. - Continued.

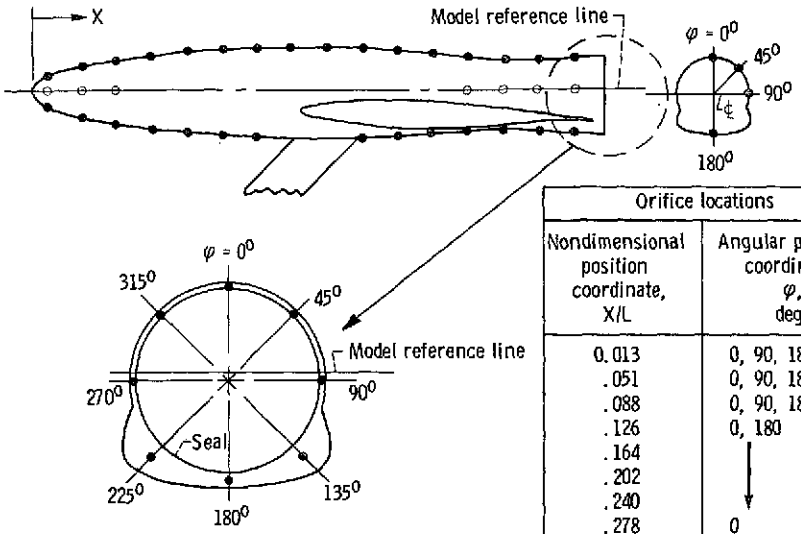

Upstream view of instrumentation in seal gap

Orifice locations	
Nondimensional position coordinate, X/L	Angular position coordinate, φ, deg
0.013	0, 90, 180
.051	0, 90, 180
.088	0, 90, 180
.126	0, 180
.164	↓
.202	
.240	
.278	0
.316	0
.354	0, 180
.392	0, 180
.430	0, 180
.468	0, 45, 90, 180
.506	↓
.544	
.582	

(d) Forward-fuselage instrumentation.

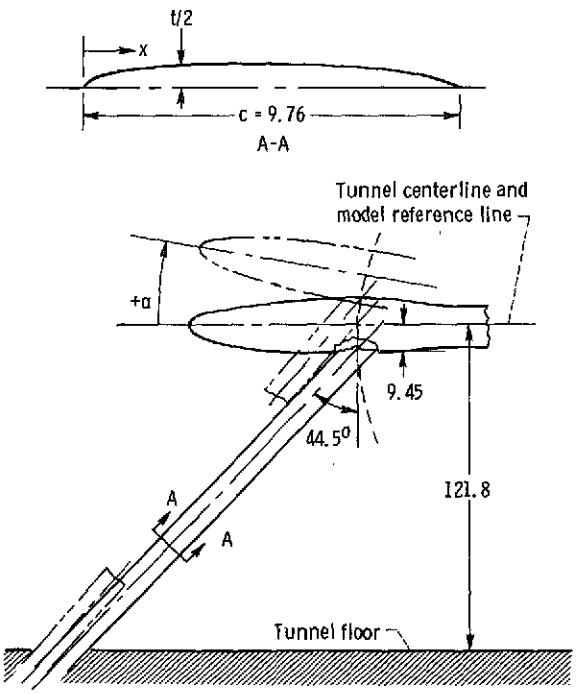

Nondimensional position coordinate, x/c	Half thickness, t/2, cm
0	0
.006	.117
.012	.183
.018	.231
.026	.272
.053	.356
.080	.417
.130	.483
.175	.521
.225	.559
.300	.597
.400	.627
.550	.632
.650	.602
.800	.498
.850	.422
.900	.320
.950	.178
1.000	0

(e) Details of forward support strut.

Figure 2. - Concluded.

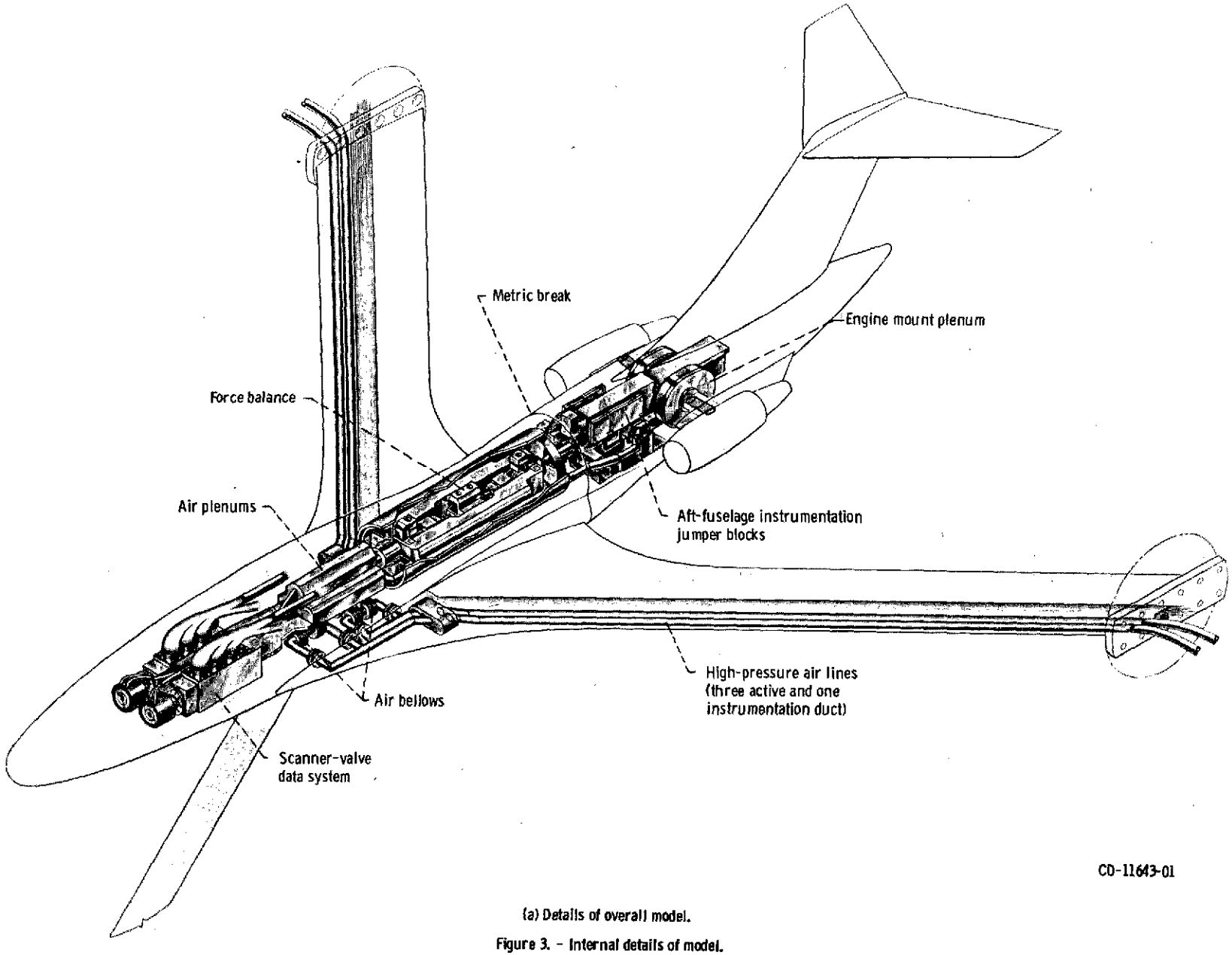

(a) Details of overall model.

Figure 3. – Internal details of model.

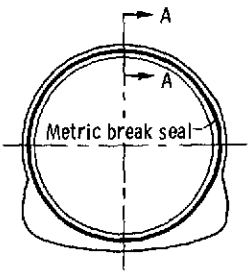

Cross section of metric break
(upstream view)

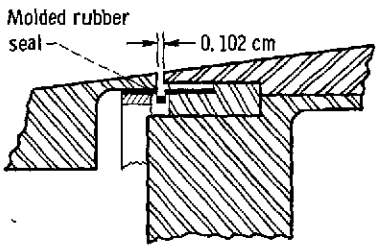

A-A

(b) Details of metric-break seal.

Figure 3. - Concluded.

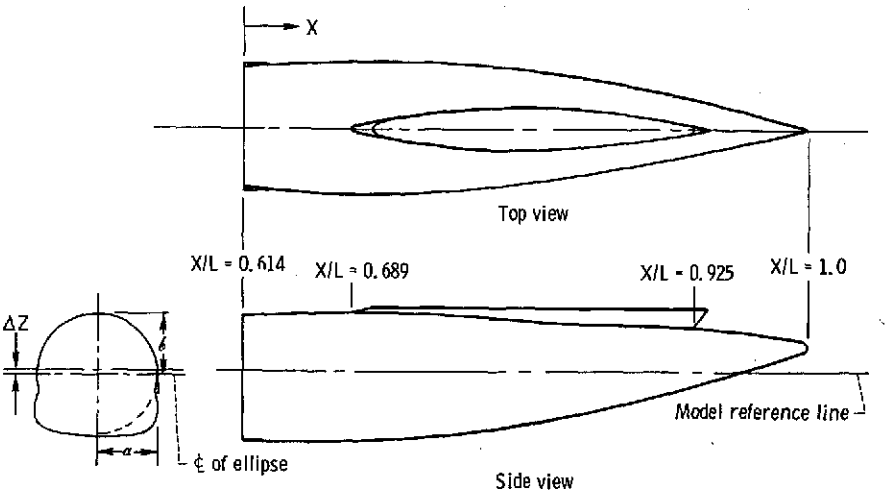

Nondimensional position coordinate, X/L	Spanwise ellipse semiaxis, a, cm	Vertical ellipse semiaxis, b, cm	Displacement of ellipse centerline from reference line, ΔZ, cm
0.614	8.284	8.284	-0.634
.634	8.530	8.566	↓
.649	8.777	8.812	↓
.667	9.024	8.883	↓
.684	9.130	8.848	↓
.702	9.221	8.848	-.589
.719	9.204	8.848	-.531
.737	9.130	8.742	-.442
.754	8.911	8.425	-.314
.772	8.626	8.389	-.130
.790	8.273	8.037	.032
.807	7.869	7.684	.231
.825	7.466	7.332	.467
.842	6.930	6.415	.753
.860	6.281	6.169	1.050
.877	5.679	5.605	1.373
.895	5.044	5.076	1.703
.912	4.371	4.406	2.013
.930	3.701	3.736	2.305
.947	2.954	3.067	2.591
.965	2.122	2.432	2.829
.982	1.146	1.762	3.081
1.000	0	0	0

(a-1) Design coordinates and sketches of fuselage.

(a) Reference fuselage.

Figure 4. - Details of aft fuselage.

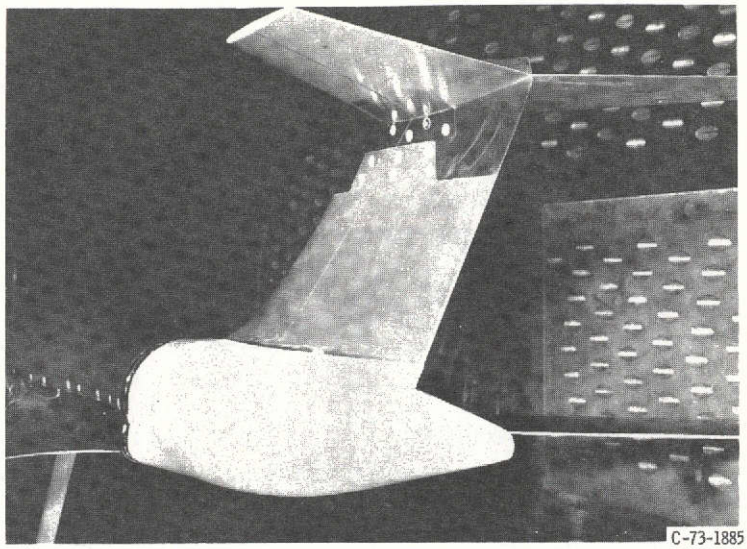

(a-2) Reference aft fuselage installed on model.

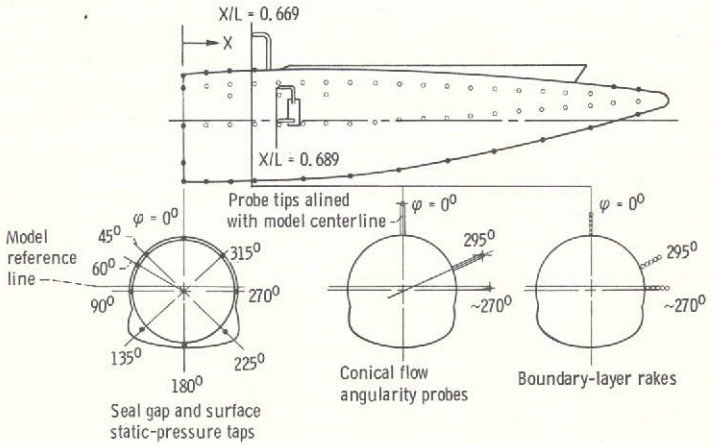

Surface orifice locations	
Nondimensional position coordinate, X/L	Angular position coordinate, φ, deg
0.633	0, 45, 90, 180
.652	0, 45, 60, 90, 180
.671	0, 45, 90, 180
.690	45, 90
.709	45, 90, 180
.728	45, 60, 90
.747	45, 90, 180
.766	45, 90
.785	45, 90, 180
.804	45, 90
.823	45, 90, 180
.842	45, 90
.861	45, 90, 180
.880	45, 90
.898	45, 90, 180
.917	45, 90
.936	45, 90, 180
.955	0, 90, 180
.974	0, 90, 180

(a-3) Instrumentation.
(a) Continued.

Figure 4. - Continued.

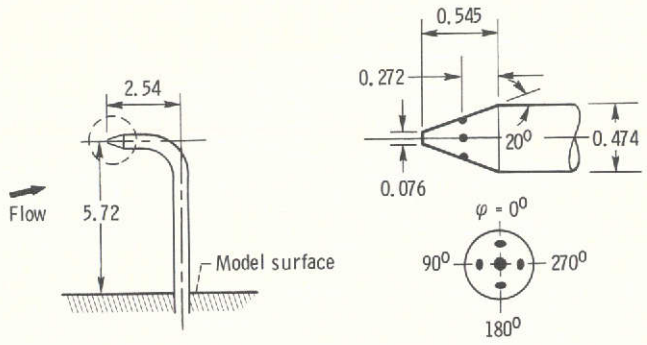

(a-4) Details of conical probe. (Dimensions are in centimeters.)

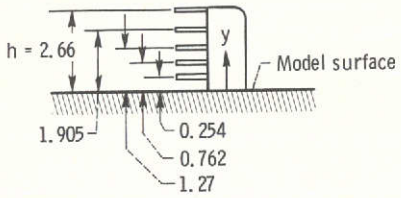

(a-5) Details of boundary-layer rake. (Dimensions are in centimeters.)

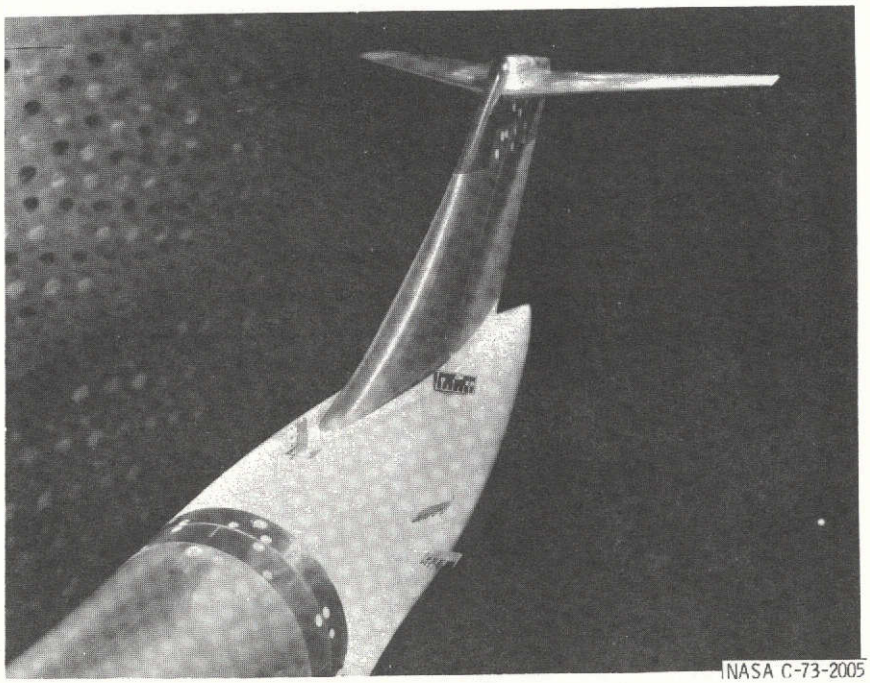

(a-6) Boundary-layer rakes installed on model.

(a) Concluded.

Figure 4. - Continued.

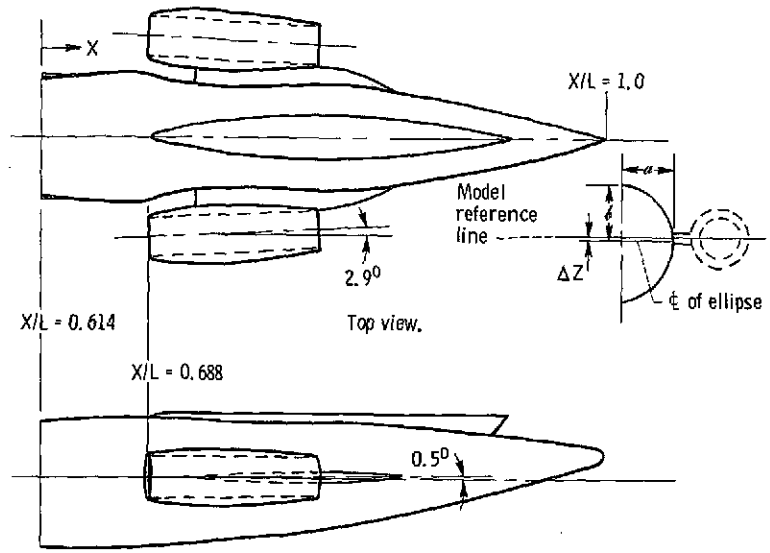

Side view

Aft-fuselage coordinates for nacelle simulated mass flow ratios m/m_0 of 0.46 and 0.6						
Nondimensional position coordinate, X/L	Spanwise ellipse semi-axis, a, cm		Vertical ellipse semi-axis, b, cm		Displacement of ellipse centerline from reference line, ΔZ, cm	
	m/m_0 = 0.46	m/m_0 = 0.6	m/m_0 = 0.46	m/m_0 = 0.6	m/m_0 = 0.46	m/m_0 = 0.6
0.614	8.284	8.284	8.284	8.284	-0.634	-0.634
.632	8.460	8.460	8.566	8.566	↓	↓
.649	8.812	8.812	8.812	8.812		
.667	9.024	9.024	8.883	8.883	↓	↓
.675	9.094	9.024	8.953	8.918	-.719	-.730
.684	9.094	8.883	9.130	8.953	-.691	-.691
.693	8.566	8.636	8.918	8.883	-.649	-.642
.702	8.072	8.360	8.812	8.848	-.620	-.599
.719	7.649	7.995	8.777	8.707	-.522	-.465
.737	7.297	7.700	8.389	8.530	-.412	-.303
.754	7.120	7.550	8.178	8.354	-.324	-.141
.772	7.156	7.529	7.931	8.072	-.233	-.007
.790	7.332	7.614	7.720	7.931	-.085	.081
.807	7.543	7.568	7.790	7.649	.183	.240
.825	7.332	7.321	7.261	7.226	.465	.465
.842	6.874	6.909	6.768	6.768	.761	.754
.860	6.274	6.274	6.274	6.274	1.050	1.050
.877	5.640	5.640	5.640	5.640	1.375	1.375
.895	5.005	5.005	5.005	5.005	1.703	1.703
.912	4.336	4.336	4.336	4.336	2.013	2.013
.930	3.701	3.701	3.701	3.701	2.305	2.305
.947	2.890	2.890	3.102	3.102	2.591	2.591
.965	2.115	2.115	2.432	2.432	2.827	2.827
.982	1.128	1.128	1.762	1.762	3.081	3.081
1.000	0	0	0	0	0	0

(b-1) Design coordinates and sketches of fuselage.

(b) Aft fuselages with flow-through nacelles.

Figure 4. - Continued.

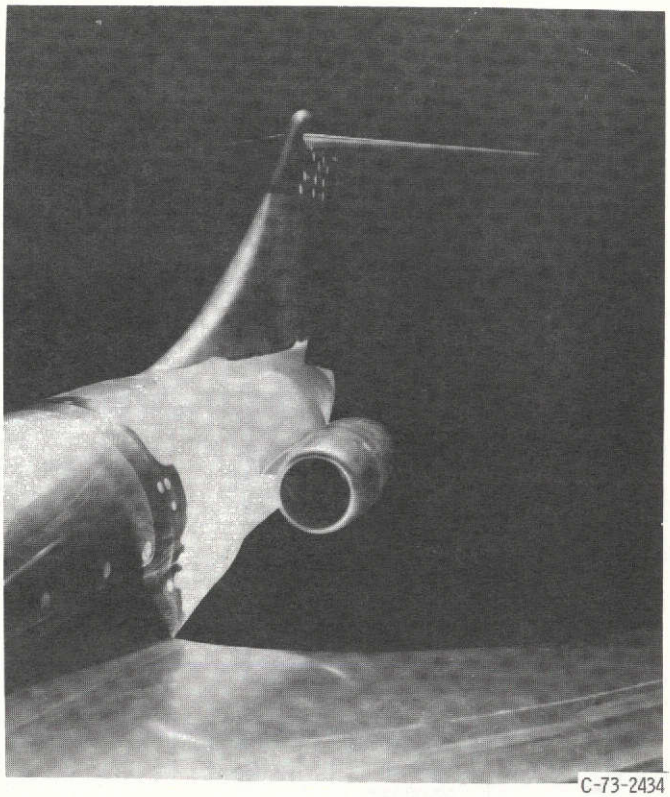

C-73-2434

(b-2) Nacelles installed on model, front view.

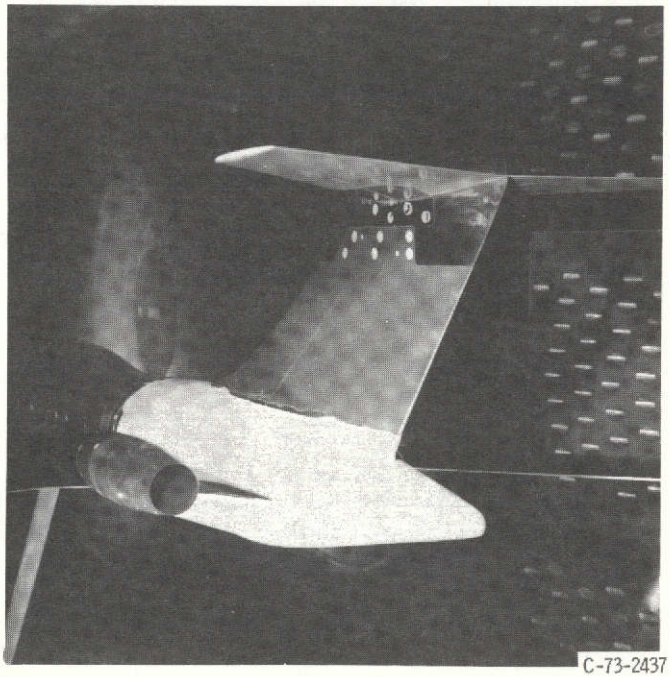

C-73-2437

(b-3) Nacelles installed on model, rear view.

(b) Continued.

Figure 4. - Continued.

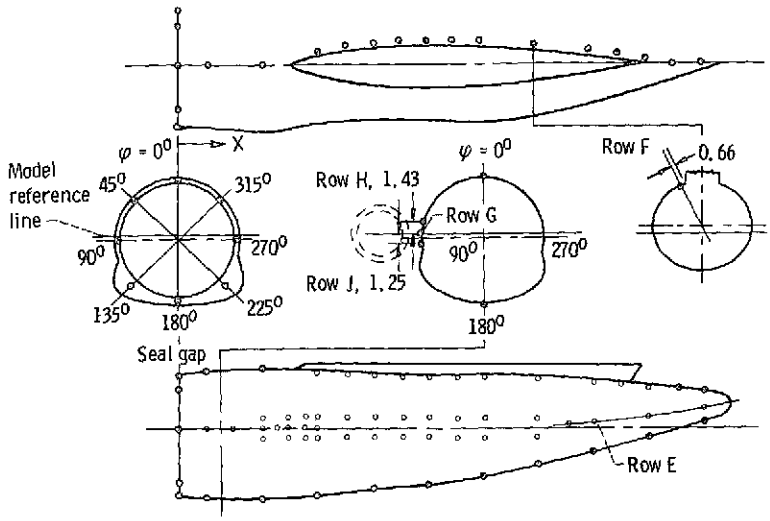

Surface orifice locations	
Nondimensional position coordinate, X/L	Angular position coordinate, φ, deg (or row)
0.634	0, 180, G
.651	G
.671	0, 180, G, H, J
.681	G
.689	G, H, J
.700	G, H, J
.709	180, F, G, H, J
.729	F, H, J
.750	180, F, H, J
.767	F, H, J
.785	180, F, H, J
.804	F, H, J
.823	180, F, H, J
.861	180, F, H, J
.879	E
.898	180, E, F
.918	F
.936	180, E, F
.955	0
.974	0, 180, E

(b-4) Details of fuselage instrumentation. (Dimensions are in centimeters.)
(b) Concluded.

Figure 4. - Concluded.

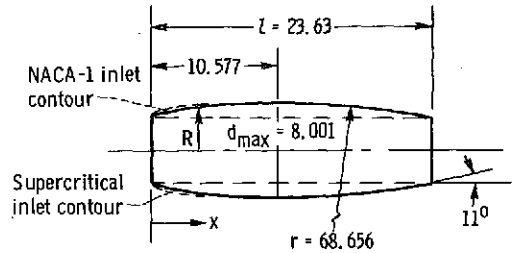

Nondimensional position coordinate, x/l		Nondimensional radial coordinate, R/l	
		NACA-1 inlet	Supercritical inlet
Inlet	0	0.116	0.116
	.004	.1215	.125
	.009	.1242	.130
	.018	.1280	.136
	.027	.131	.140
	.045	.1354	.145
	.067	.140	.149
	.090	.144	.153
	.112	.148	.155
	.134	.151	.157
	.157	.153	.159
	.201	.158	.162
	.251	.162	.164
	.313	.166	.166
	.385	.169	.169
	.448	.1693	.1693
Boattail	.501	.1688	.1688
	.609	.165	.165
	.716	.157	.157
	.824	.145	.145
	.931	.129	.129
	1.000	.116	.116

(a) Flow-through nacelles with simulated mass flow ratio, m/m_0 = 0.46.

Figure 5. - Details of nacelles and pylon.

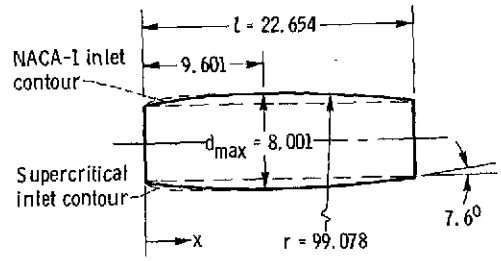

Nondimensional position coordinate, x/ℓ		Nondimensional radial coordinate, R/ℓ	
		NACA-1 inlet	Supercritical inlet
Inlet	0	0.1385	0.1385
	.0034	.142	.144
	.009	.144	.148
	.017	.147	.152
	.026	.1488	.155
	.042	.152	.159
	.064	.1555	.162
	.085	.1585	.165
	.106	.161	.166
	.127	.164	.168
	.148	.166	.169
	.170	.1675	.170
	.191	.169	.171
	.214	.1705	.172
	.237	.172	.173
	.263	.173	.174
	.297	.1742	.1744
	.331	.1753	.1753
	.364	.1760	.1760
	.424	.1766	.1766
Boattail	.480	.1762	.1762
	.592	.173	.173
	.704	.168	.168
	.816	.159	.159
	.928	.147	.147
	.984	.140	.140
	1.000	.1385	.1385

(b) Flow-through nacelles with simulated mass flow ratio, $m/m_0 = 0.6$.

Figure 5. - Continued.

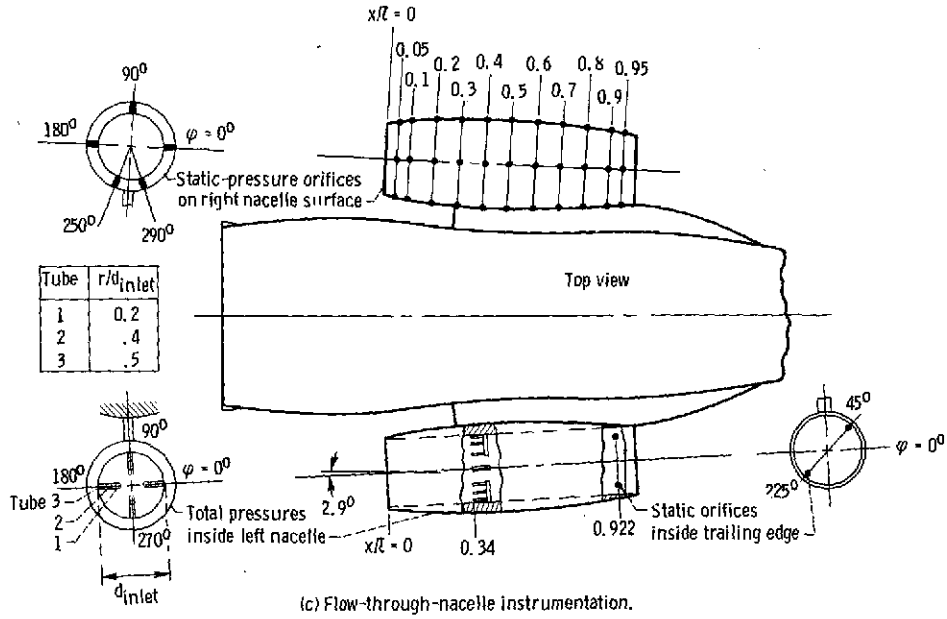

Tube	r/d_{inlet}
1	0.2
2	.4
3	.5

(c) Flow-through-nacelle instrumentation.

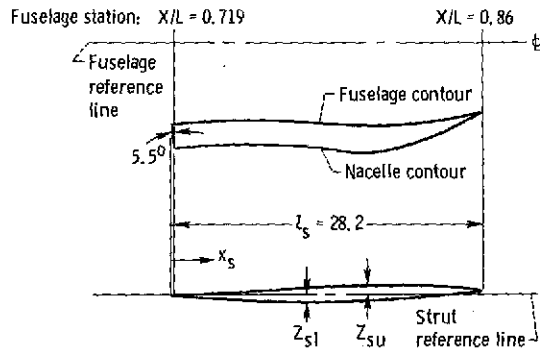

Nondimensional position coordinate, x_s/ℓ_s	Strut upper coordinate, Z_{su}, cm	Strut lower coordinate, Z_{sl}, cm
0	0	0
.031	.053	-.106
.062	.106	-.194
.125	.194	-.335
.187	.300	-.423
.250	.388	-.511
.312	.458	-.564
.375	.546	-.592
.437	.634	-.599
.500	.723	-.599
.562	.793	-.575
.625	.850	-.518
.687	.892	-.430
.750	.909	-.342
.812	.874	-.236
.875	.811	-.095
.938	.691	.081
.969	.585	.204
1.000	.416	.416

(d) Details of nacelle pylon.

Figure 5. - Concluded.

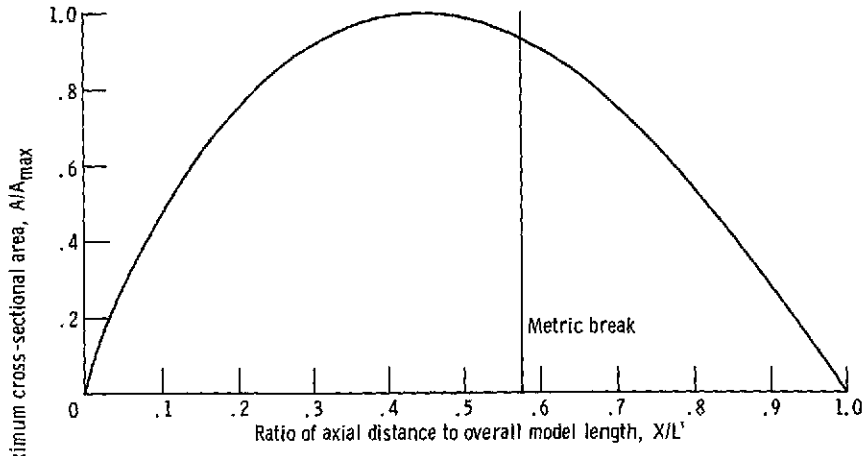

(a) Overall design-area envelope.

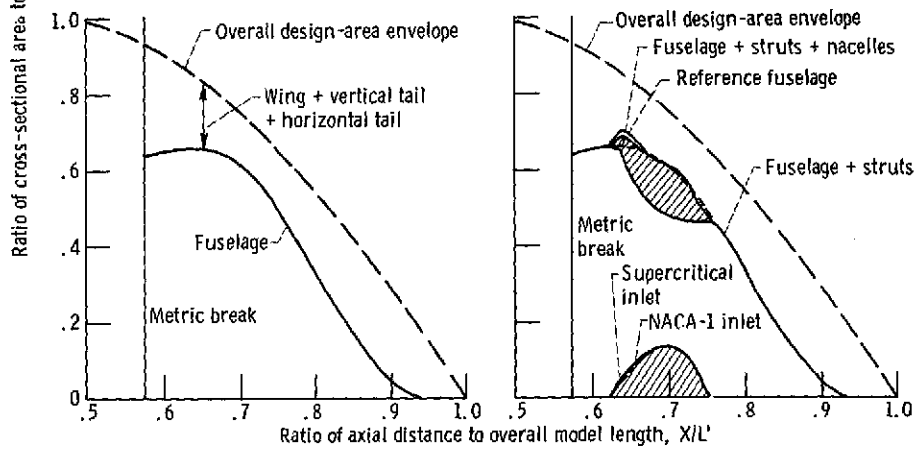

(b-1) Reference fuselage.

(b-2) Fuselage with flow-through nacelles and simulated mass flow ratio, $m/m_0 = 0.46$.

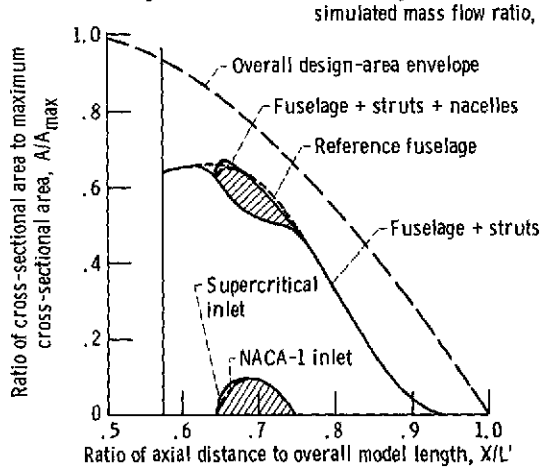

(b-3) Fuselage with flow-through nacelles and simulated mass flow ratio, $m/m_0 = 0.6$.

(b) Aft-fuselage area distributions.

Figure 6. - Design envelope and details of model area distribution.

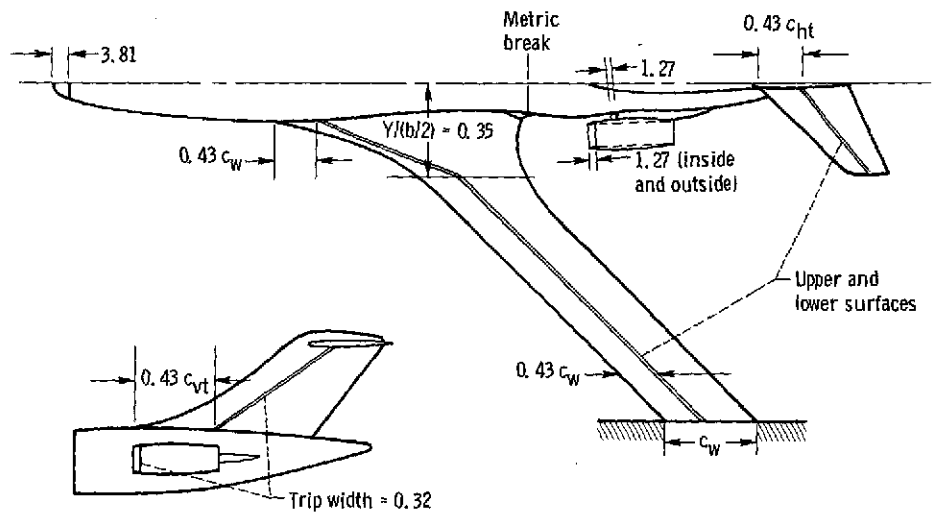

Figure 7. - Boundary-layer transition strip locations. Grit size: upstream of metric break, no. 80; downstream of metric break, no. 120. (Dimensions are in centimeters.)

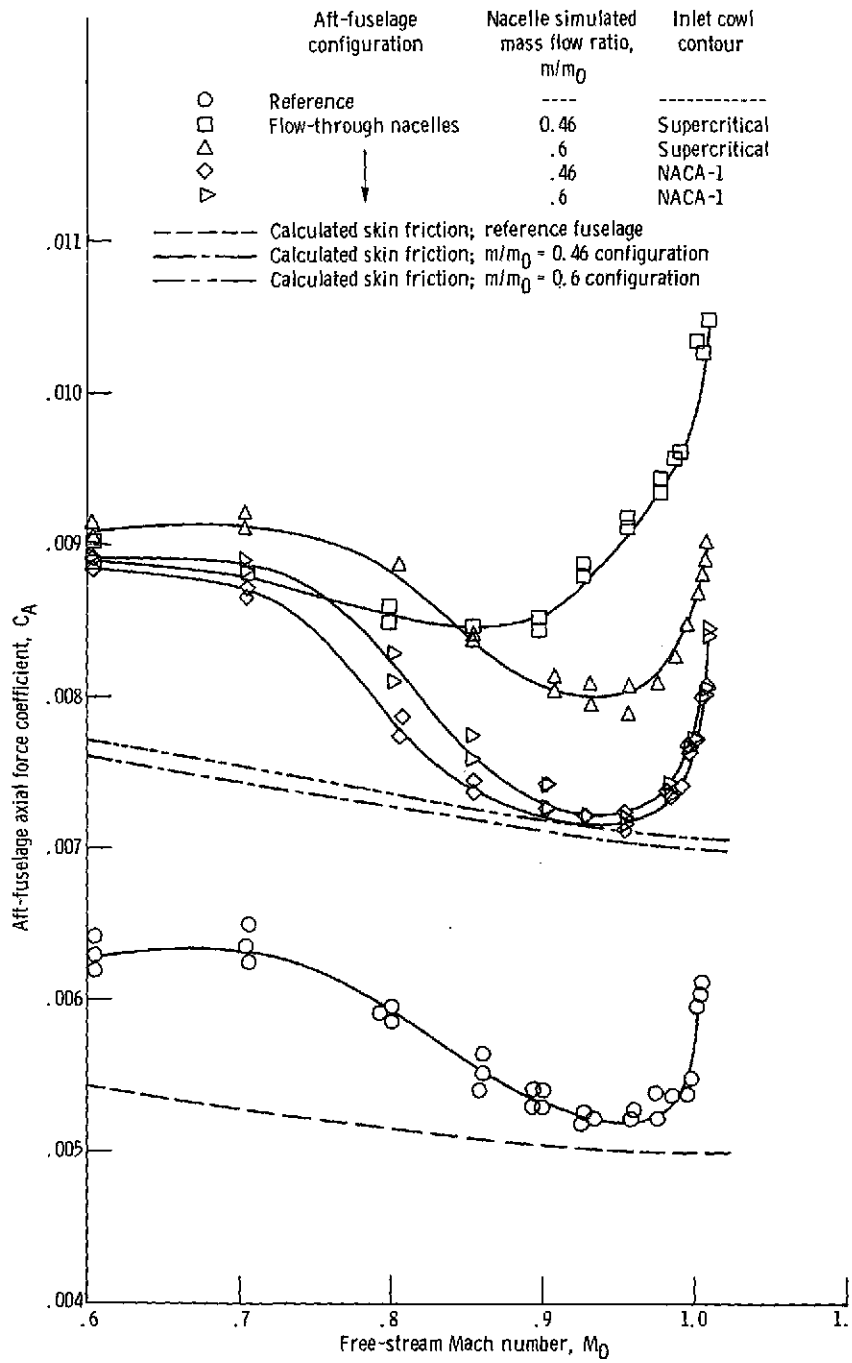

Figure 8. - Comparison of reference and flow-through-nacelle aft-fuselage axial force coefficients. Model angle of attack, $\alpha = 3.2^{\circ}$.

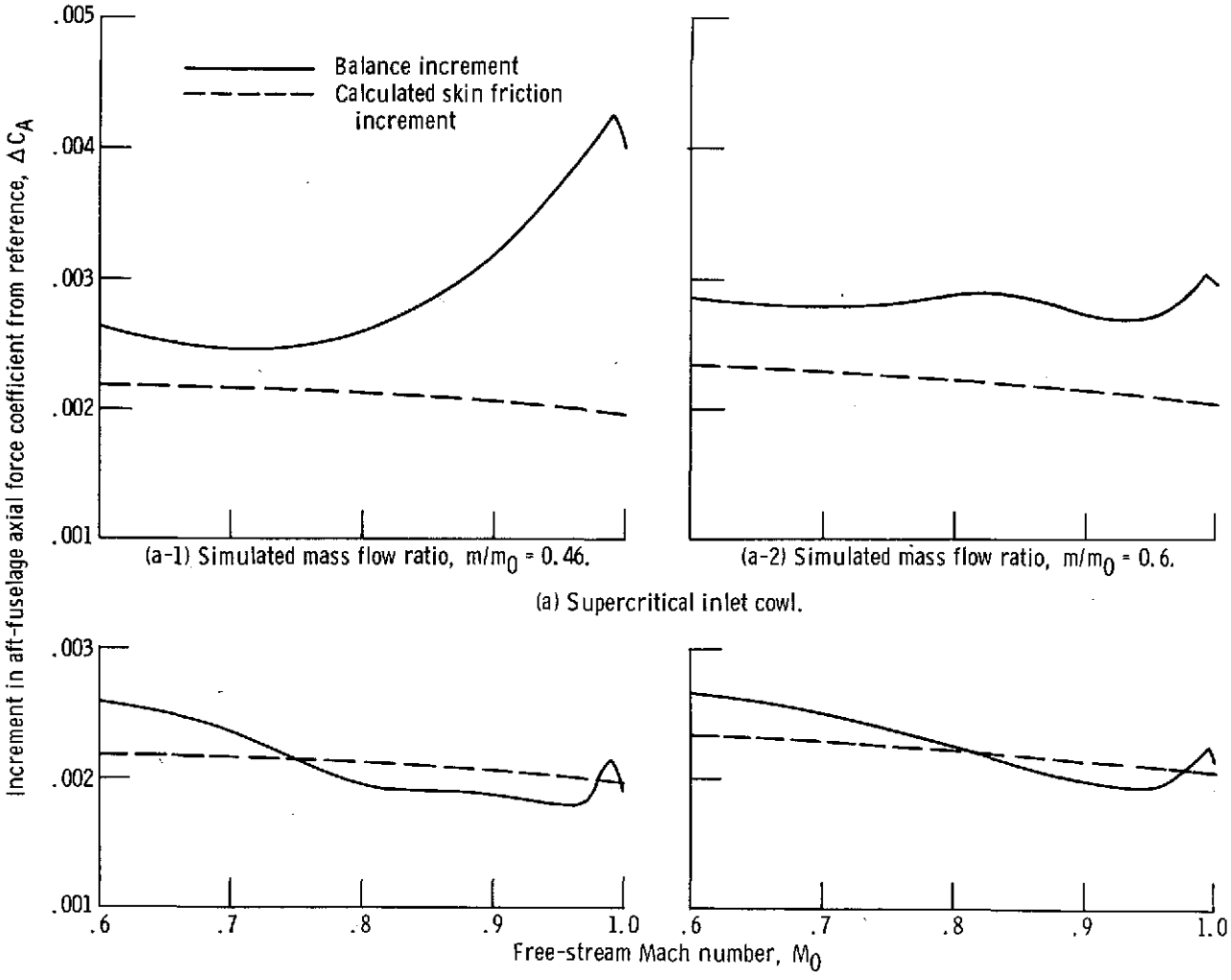

(a-1) Simulated mass flow ratio, $m/m_0 = 0.46$.

(a-2) Simulated mass flow ratio, $m/m_0 = 0.6$.

(a) Supercritical inlet cowl.

(b-1) Simulated mass flow ratio, $m/m_0 = 0.46$.

(b-2) Simulated mass flow ratio, $m/m_0 = 0.6$.

(b) NACA-1 inlet cowl.

Figure 9. - Variation of increment in aft-fuselage axial force coefficient from the reference configuration with free-stream Mach number; model angle of attack, $\alpha = 3.2^{\circ}$.

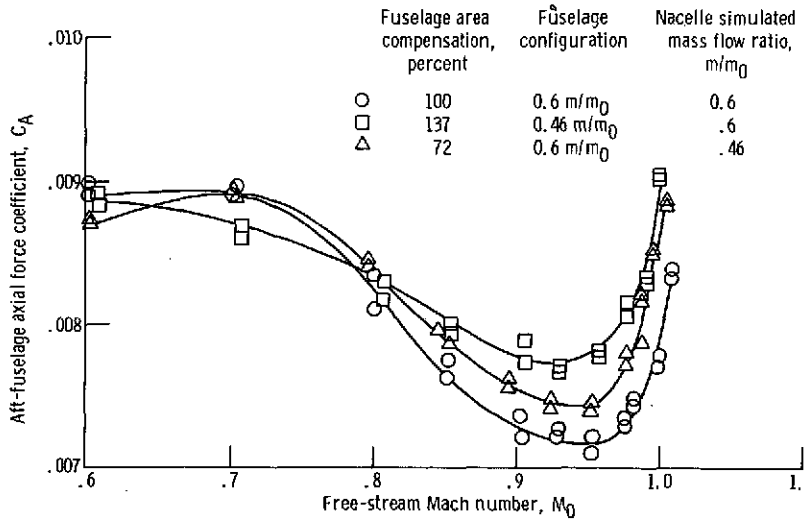

Figure 10. - Effect of local area ruling on aft-fuselage axial force coefficient with flow-through nacelles. NACA-1 inlet; model angle of attack, $\alpha = 3.2^0$.

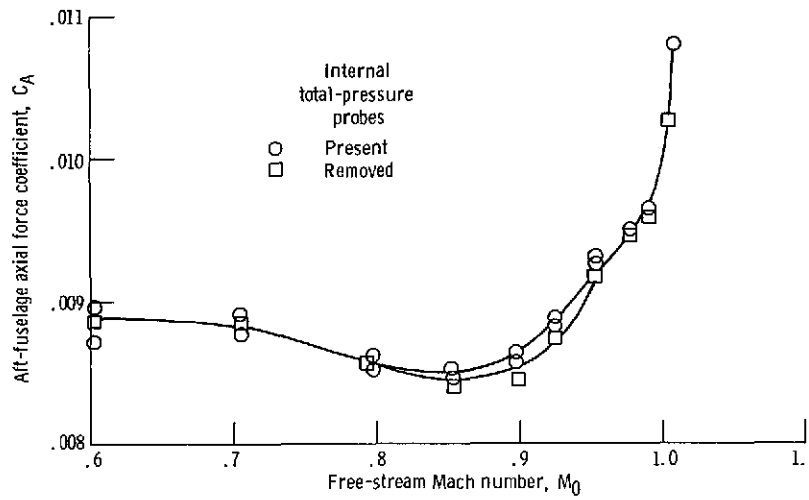

Figure 11. - Effect of nacelle internal total-pressure probes on aft-fuselage axial force coefficient. Supercritical inlet cowl; nacelle simulated mass flow ratio, $m/m_0 = 0.46$; model angle of attack, $\alpha = 3.2^0$.

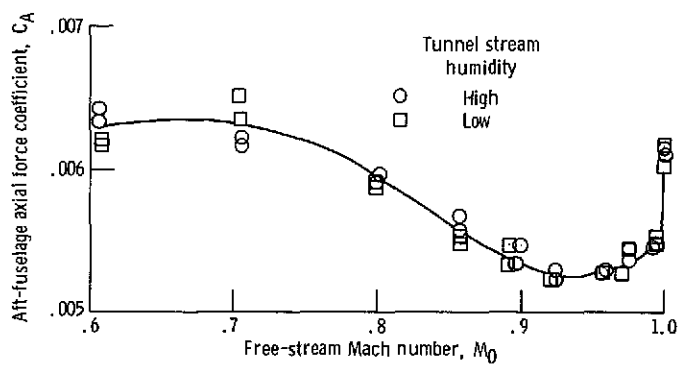

Figure 12. - Effect of tunnel-stream humidity on aft-fuselage axial force coefficient. Reference fuselage; model angle of attack, $\alpha = 3.2^0$.

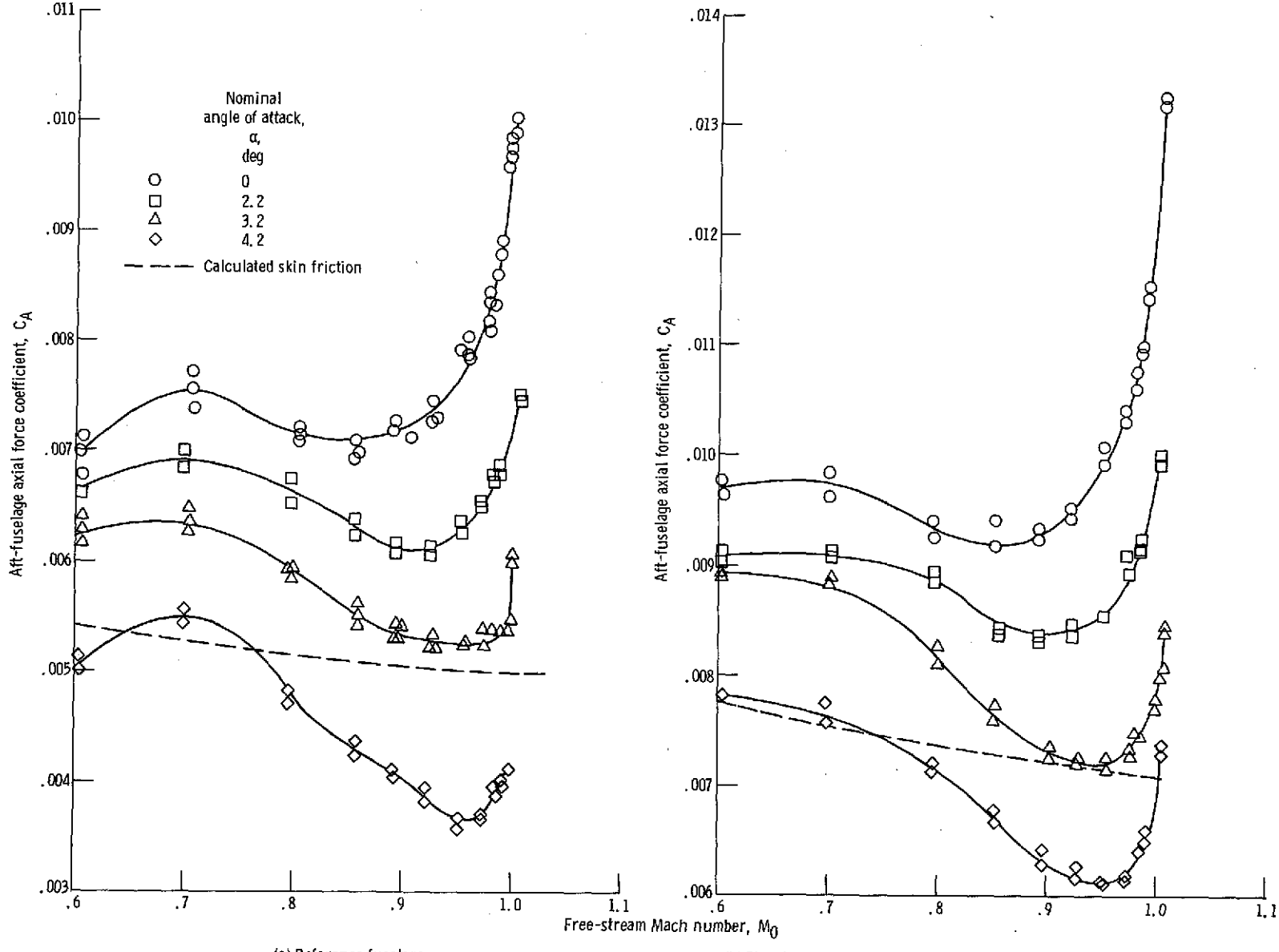

(a) Reference fuselage.

(b) Flow-through nacelles with NACA-1 inlet contour and simulated mass flow ratio, $m/m_0 = 0.6$.

Figure 13. - Effect of angle of attack on aft-fuselage axial force coefficient.

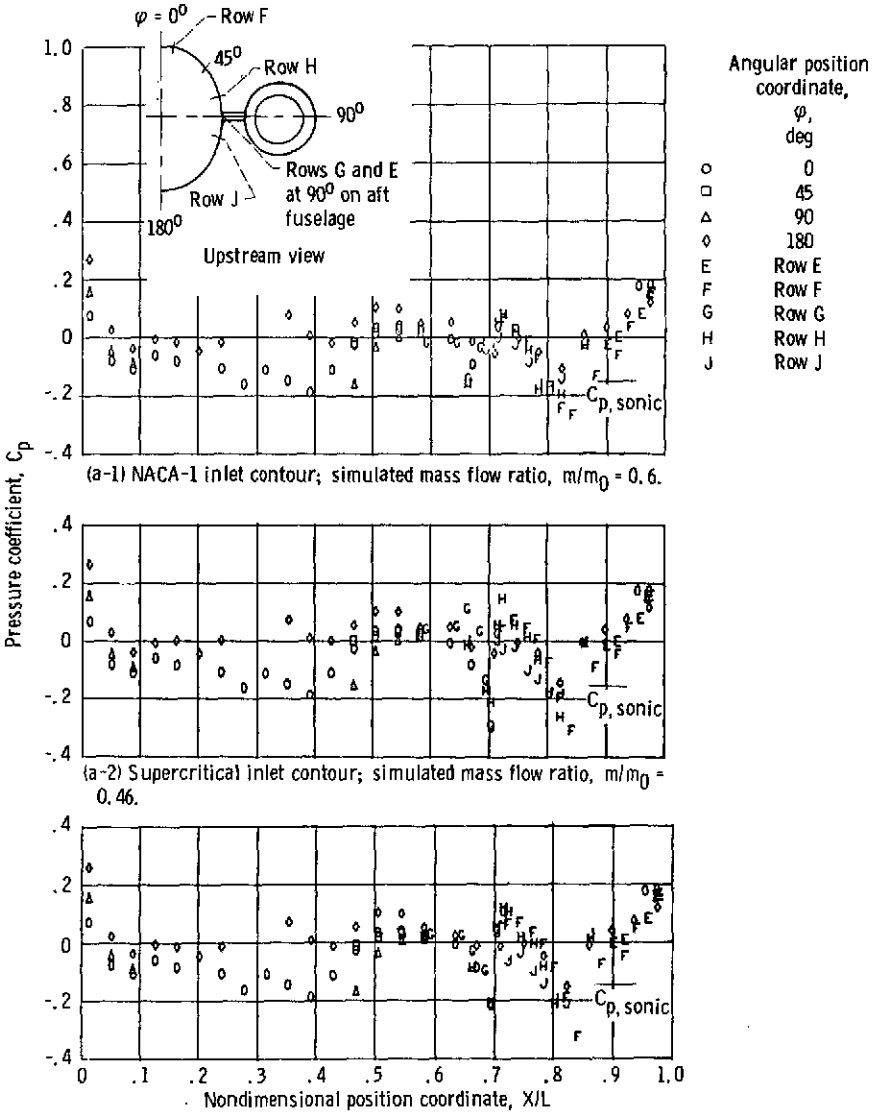

(a-1) NACA-1 inlet contour; simulated mass flow ratio, $m/m_0 = 0.6$.

(a-2) Supercritical inlet contour; simulated mass flow ratio, $m/m_0 = 0.46$.

(a-3) NACA-1 inlet contour; simulated mass flow ratio, $m/m_0 = 0.46$.

(a) Free-stream Mach number, $M_0 = 0.92$.

Figure 14. - Effect of nacelle inlet external lip contour on fuselage pressures. Model angle of attack, $\alpha = 3.2^0$.

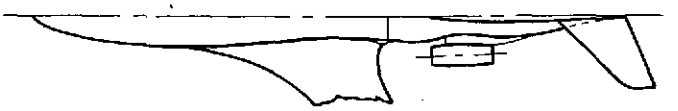

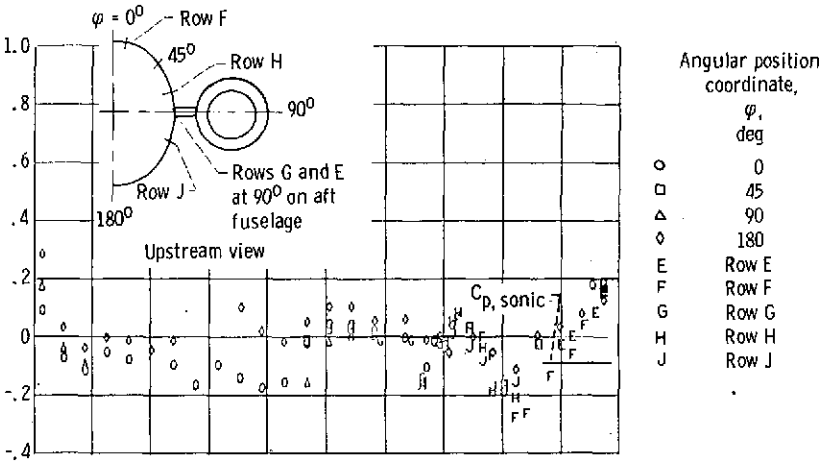

(b-1) NACA-1 inlet contour; simulated mass flow ratio, $m/m_0 = 0.6$.

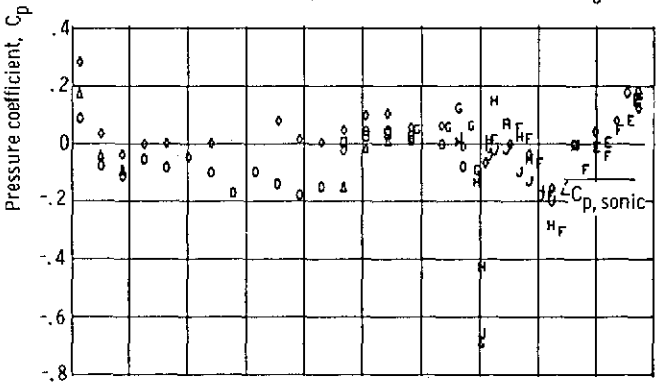

(b-2) Supercritical inlet contour; simulated mass flow ratio, $m/m_0 = 0.46$.

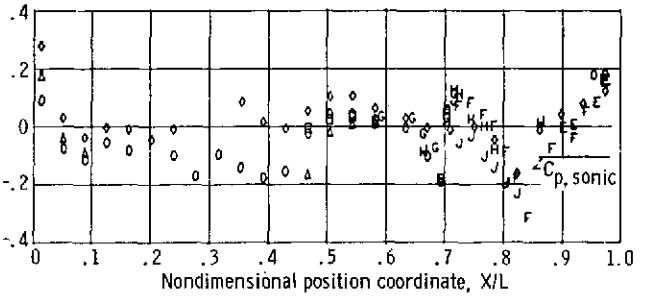

(b-3) NACA-1 inlet contour; simulated mass flow ratio, $m/m_0 = 0.46$.

(b) Free-stream Mach number, $M_0 = 0.95$.

Figure 14. - Continued.

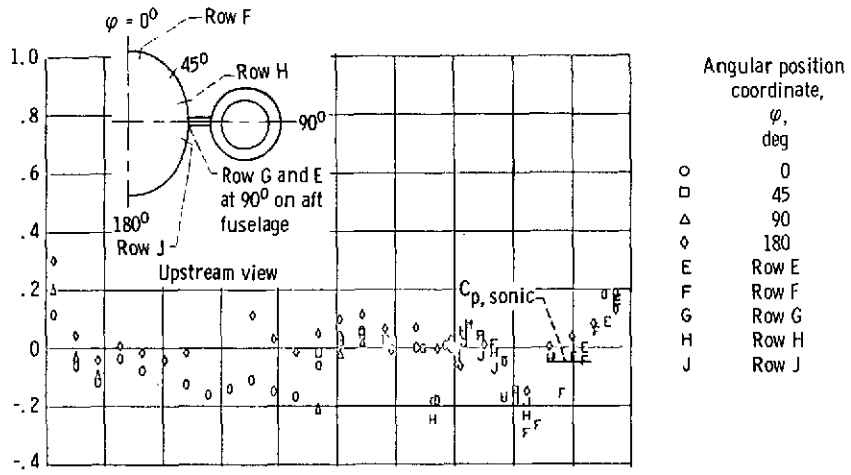

(c-1) NACA-1 inlet contour; simulated mass flow ratio, $m/m_0 = 0.6$.

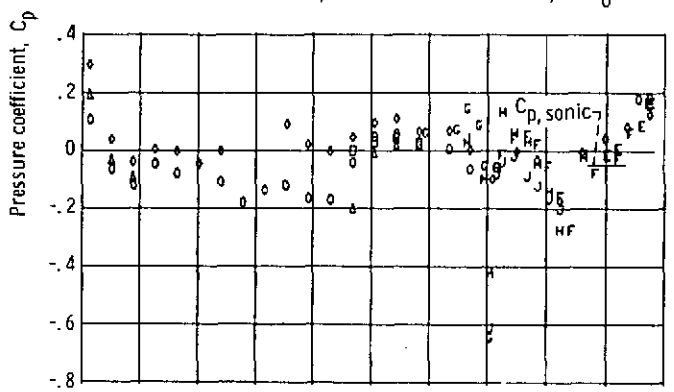

(c-2) Supercritical inlet contour; simulated mass flow ratio, $m/m_0 = 0.46$.

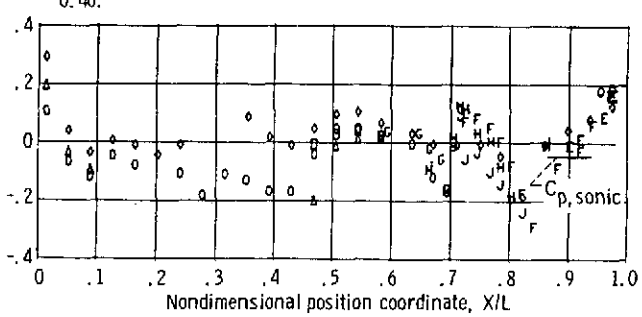

(c-3) NACA-1 inlet contour; simulated mass flow ratio, $m/m_0 = 0.46$.

(c) Free-stream Mach number, $M_0 = 0.97$.

Figure 14. - Concluded.

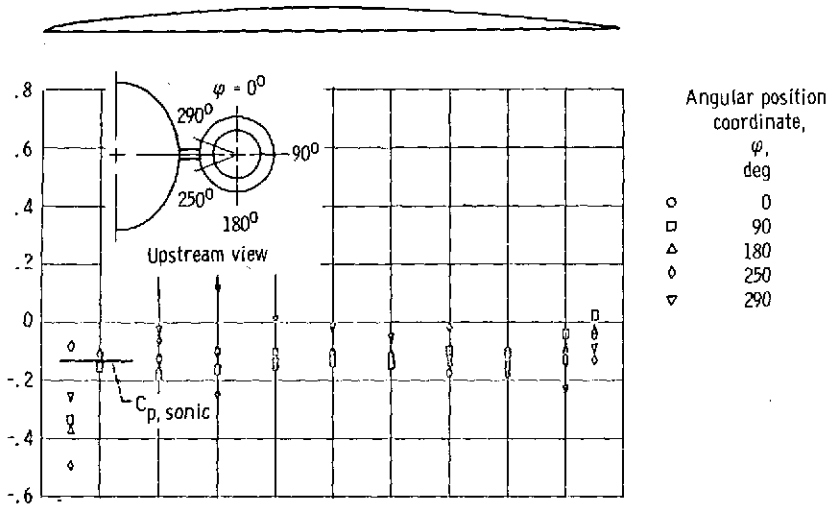

(a-1) NACA-1 inlet contour; simulated mass flow ratio, $m/m_0 = 0.6$.

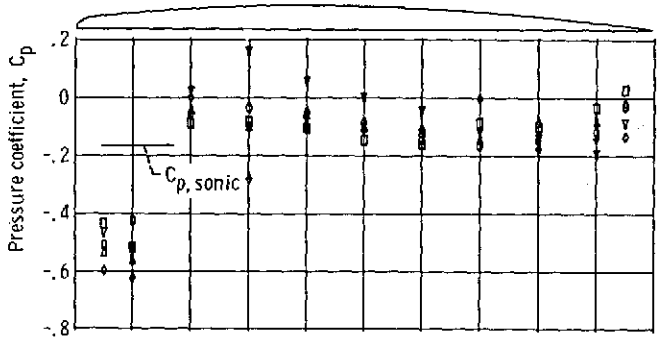

(a-2) Supercritical inlet contour; simulated mass flow ratio, $m/m_0 = 0.6$.

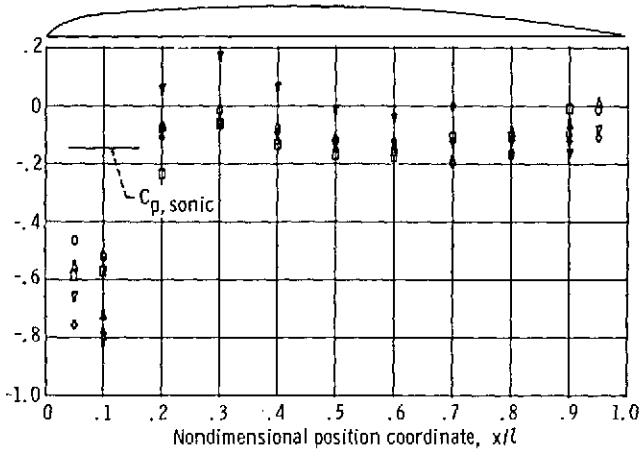

(a-3) Supercritical inlet contour; simulated mass flow ratio, $m/m_0 = 0.46$.

(a) Free-stream Mach number, $M_0 = 0.92$.

Figure 15. - Comparison of nacelle pressures. Model angle of attack, $\alpha = 3.2^\circ$.

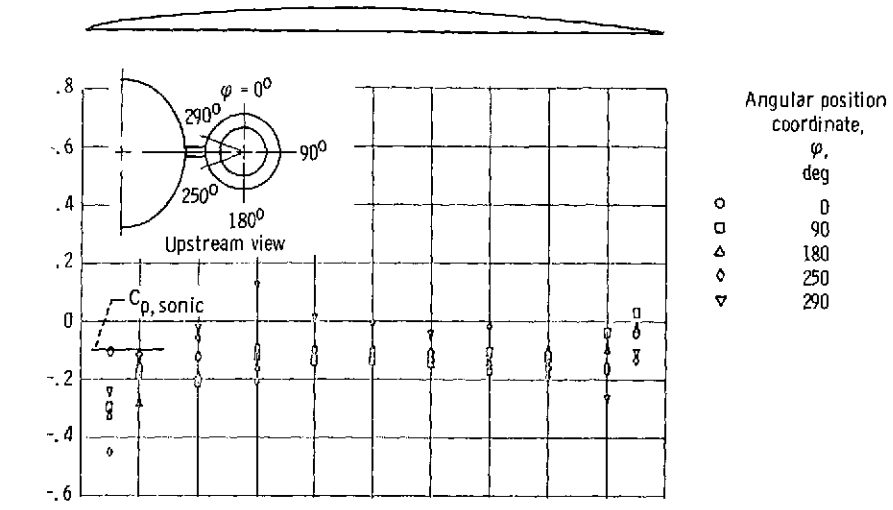

(b-1) NACA-1 inlet contour; simulated mass flow ratio, $m/m_0 = 0.6$.

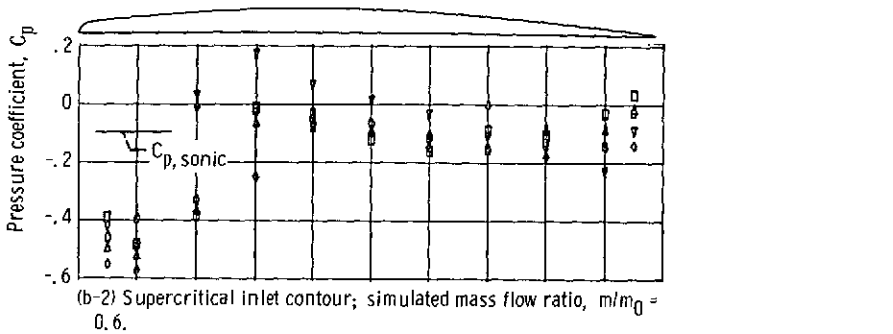

(b-2) Supercritical inlet contour; simulated mass flow ratio, $m/m_0 = 0.6$.

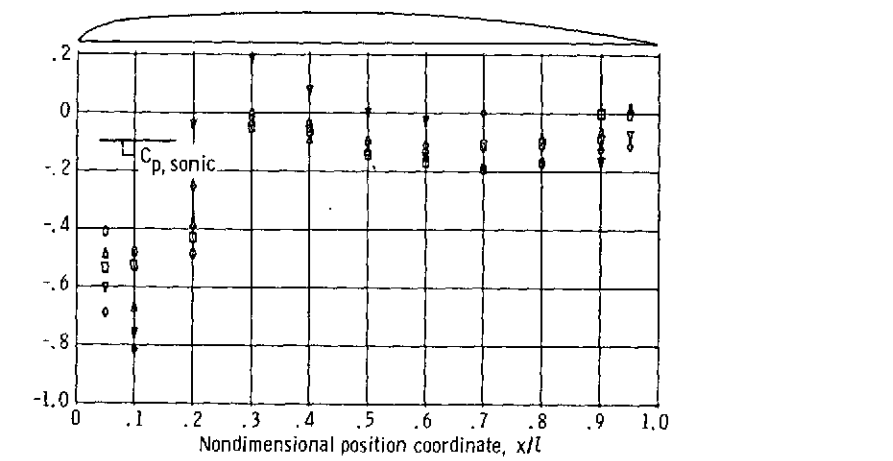

(b-3) Supercritical inlet contour; simulated mass flow ratio, $m/m_0 = 0.46$.

(b) Free-stream Mach number, $M_0 = 0.95$.

Figure 15. - Continued.

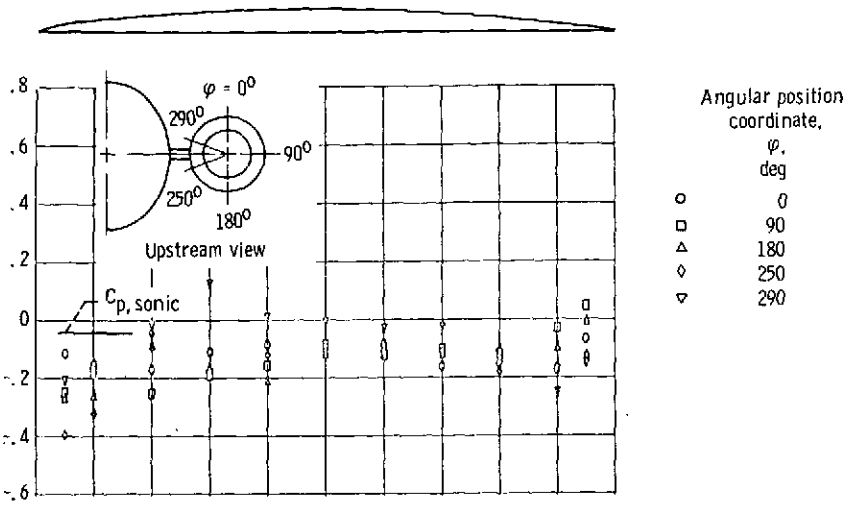

(c-1) NACA-1 inlet contour; simulated mass flow ratio, m/m_0 = 0.6.

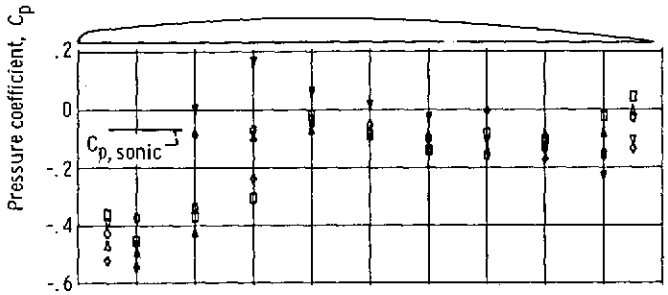

(c-2) Supercritical inlet contour; simulated mass flow ratio, m/m_0 = 0.6.

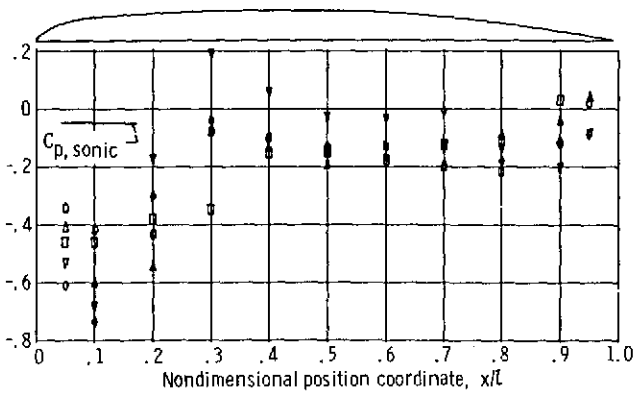

(c-3) Supercritical inlet contour; simulated mass flow ratio, m/m_0 = 0.46.

(c) Free-stream Mach number, M_0 = 0.97.

Figure 15. - Concluded.

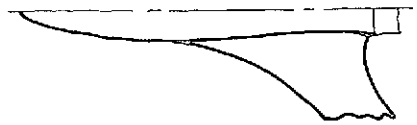

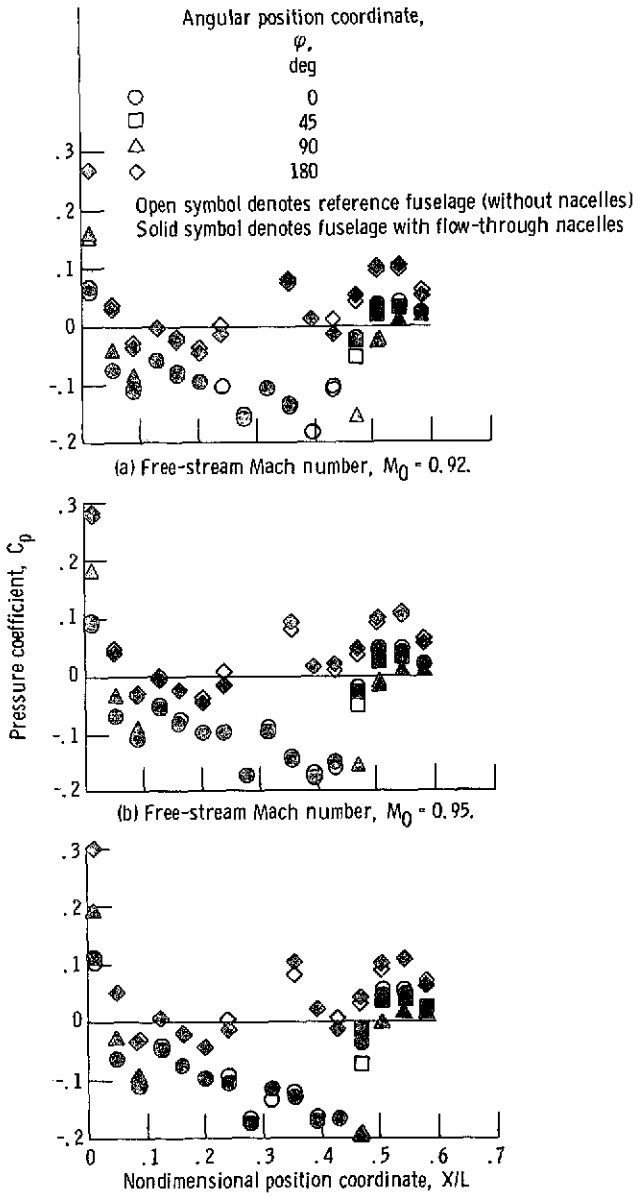

(a) Free-stream Mach number, $M_0 = 0.92$.

(b) Free-stream Mach number, $M_0 = 0.95$.

(c) Free-stream Mach number, $M_0 = 0.97$.

Figure 16. - Effect of nacelles on forward-fuselage pressures. NACA-1 inlet contour with simulated mass flow ratio, $m/m_0 = 0.6$; model angle of attack, $\alpha = 3.2^0$.

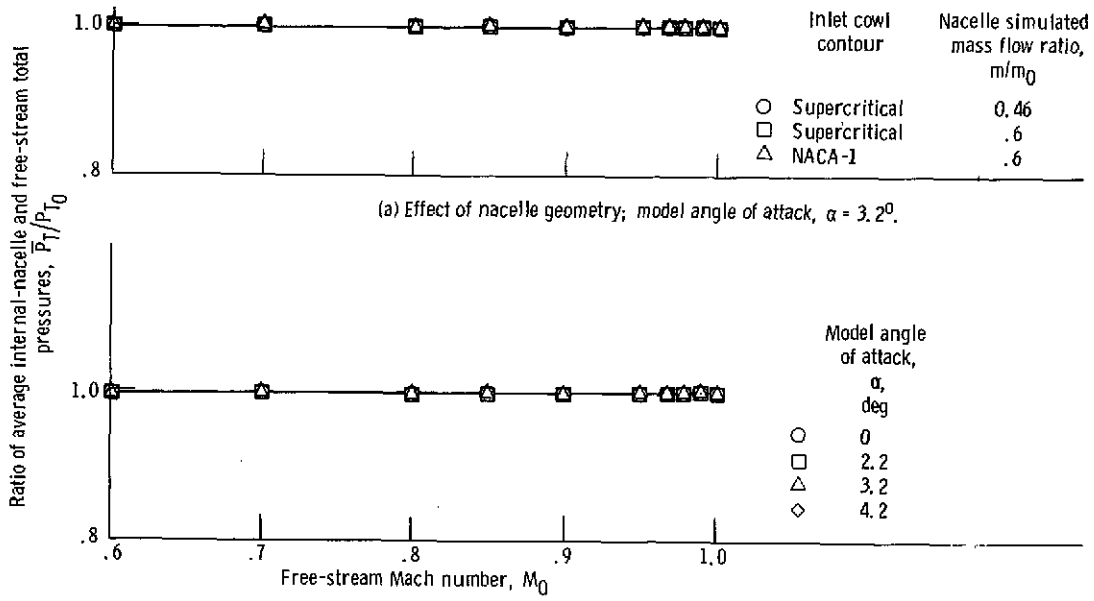

(a) Effect of nacelle geometry; model angle of attack, $\alpha = 3.2^0$.

(b) Effect of model angle of attack; NACA-1 inlet contour nacelle with simulated mass flow ratio, $m/m_0 = 0.6$.

Figure 17. - Effect of nacelle geometry and model angle of attack on average internal nacelle total pressure recovery.

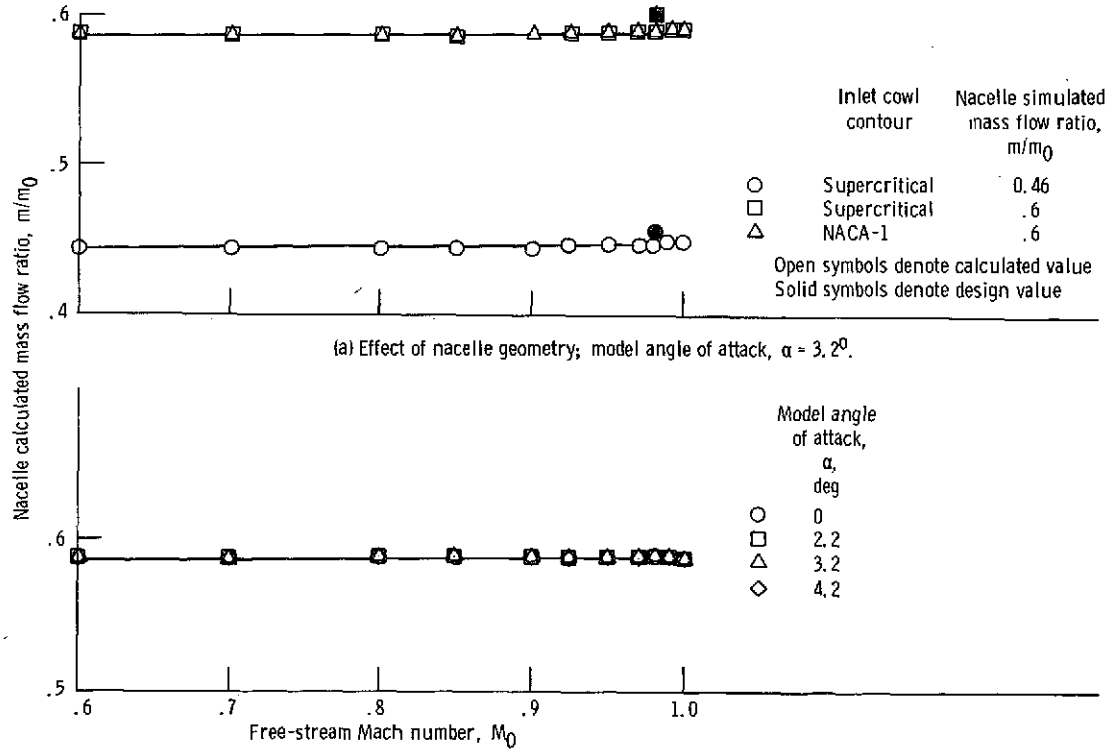

(a) Effect of nacelle geometry; model angle of attack, $\alpha = 3.2^0$.

(b) Effect of model angle of attack; NACA-1 inlet contour with simulated mass flow ratio, $m/m_0 = 0.6$.

Figure 18. - Effect of nacelle geometry and model angle of attack on nacelle calculated mass flow ratio.

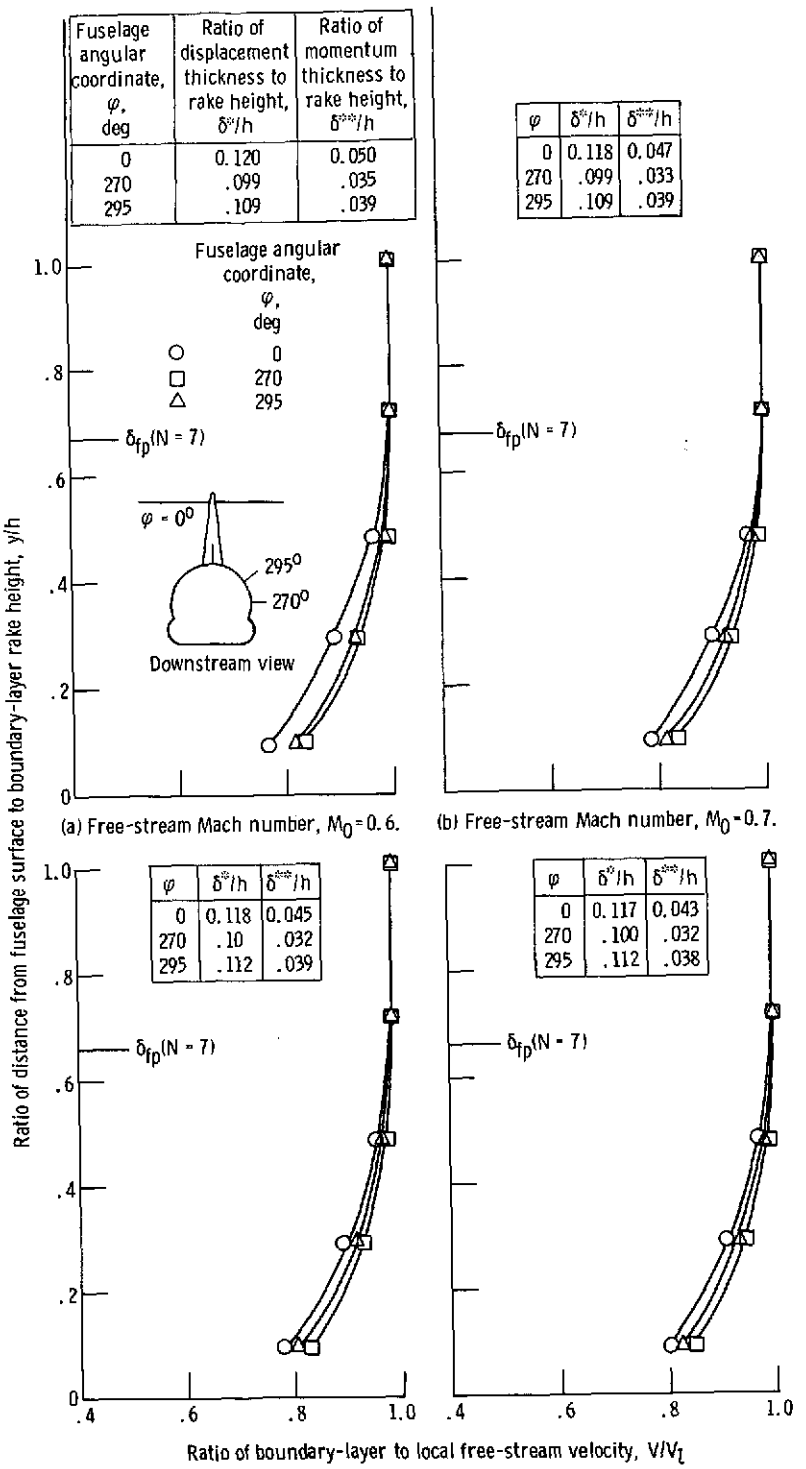

Figure 19. - Effect of free-stream Mach number on reference aft-fuselage boundary-layer velocity profiles for model cruise angle of attack, $\alpha = 3.2^{0}$.

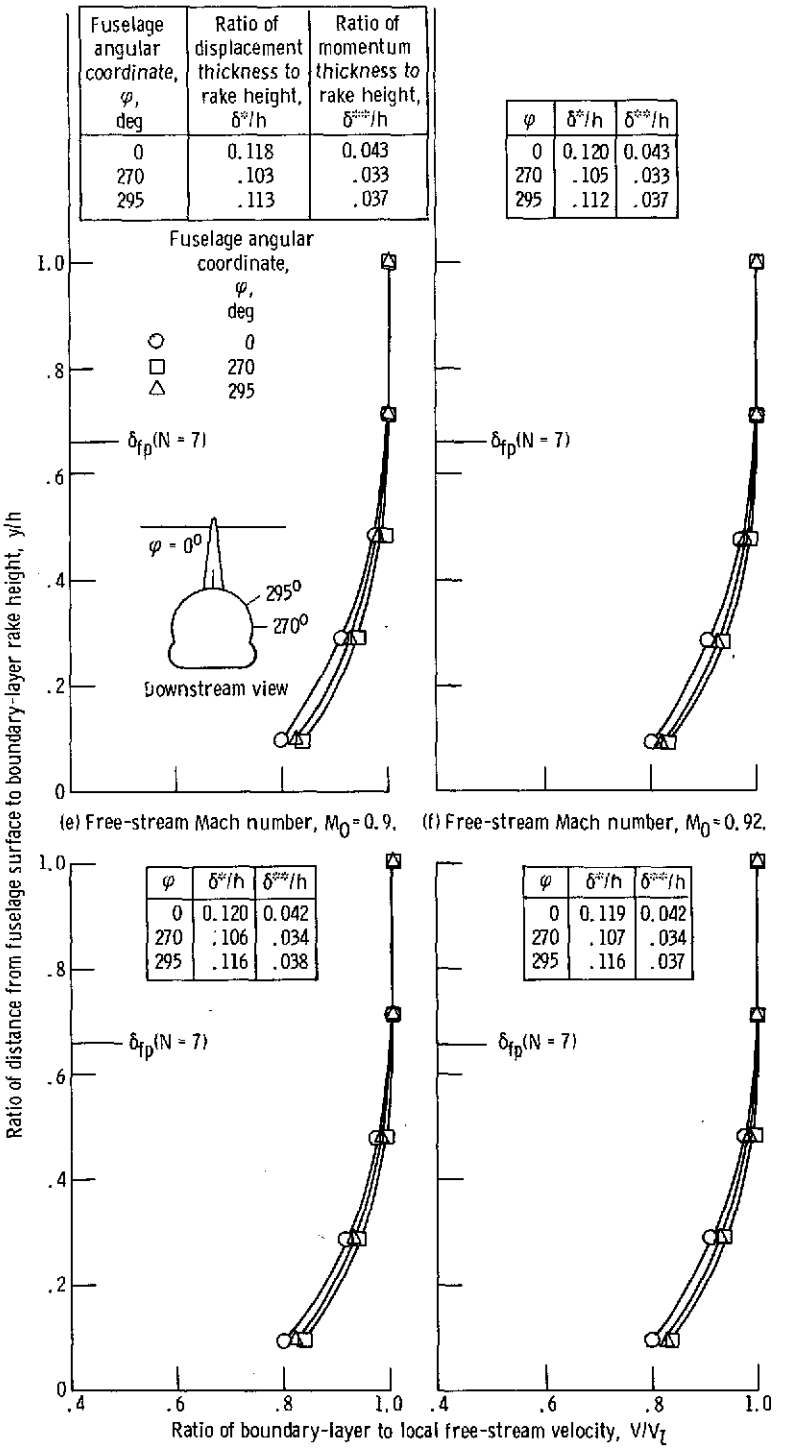

Figure 19. - Continued.

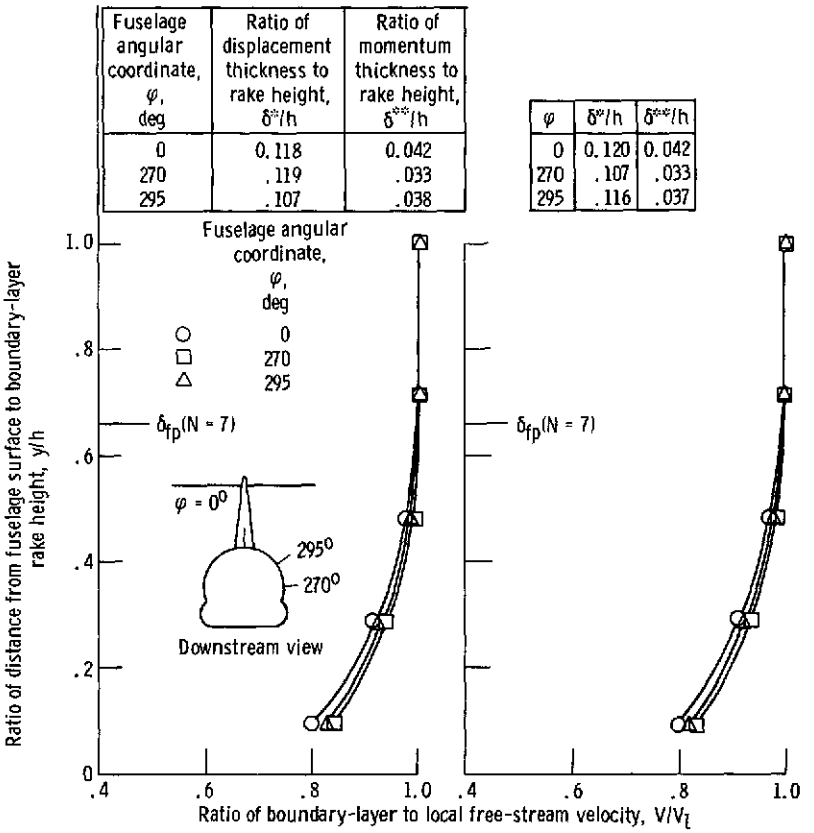

(i) Free-stream Mach number, $M_0 = 0.98$. (j) Free-stream Mach number, $M_0 = 0.99$.

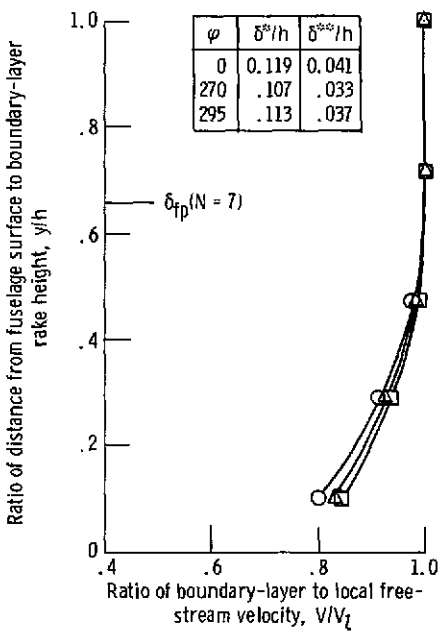

(k) Free-stream Mach number, $M_0 = 1.00$.

Figure 19. - Concluded.

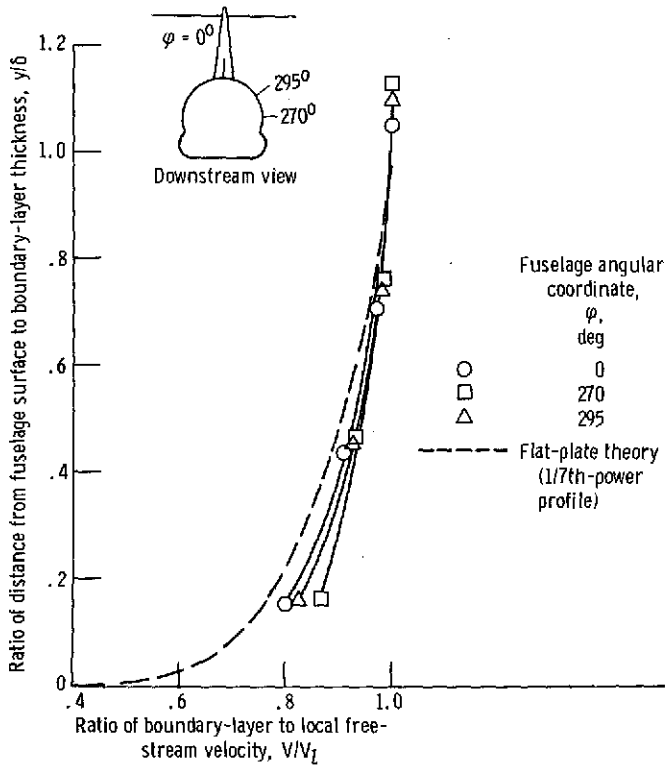

Figure 20. - Typical reference aft-fuselage boundary-layer velocity profiles for model angle of attack, $\alpha = 3.2^0$, at a free-stream Mach number of 0.97.

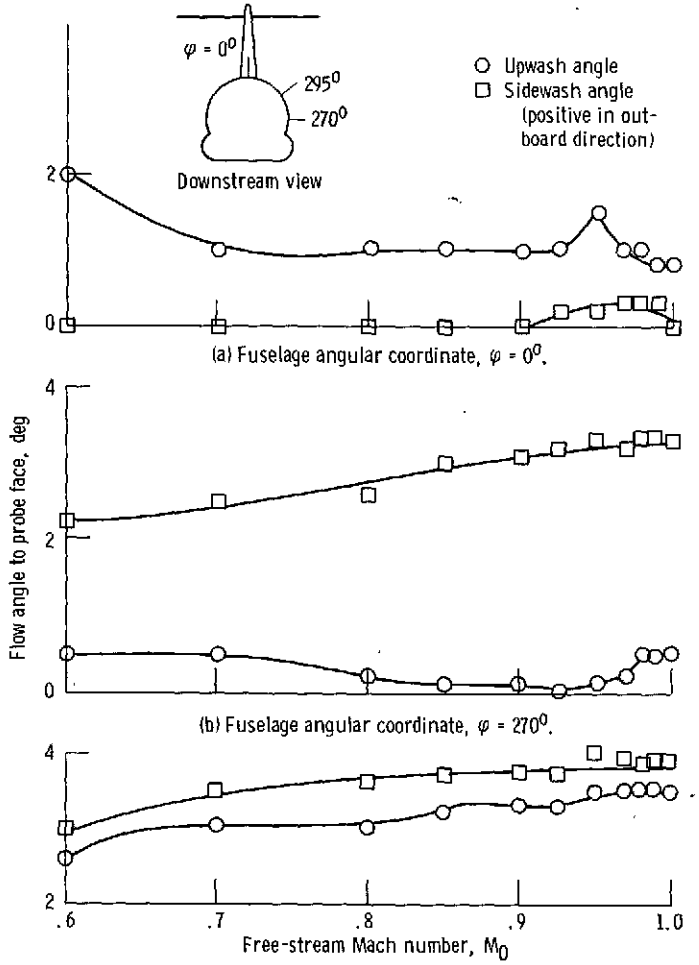

Figure 21. - Local flow angles to probe face. Model angle of attack, $\alpha = 3.2^0$.

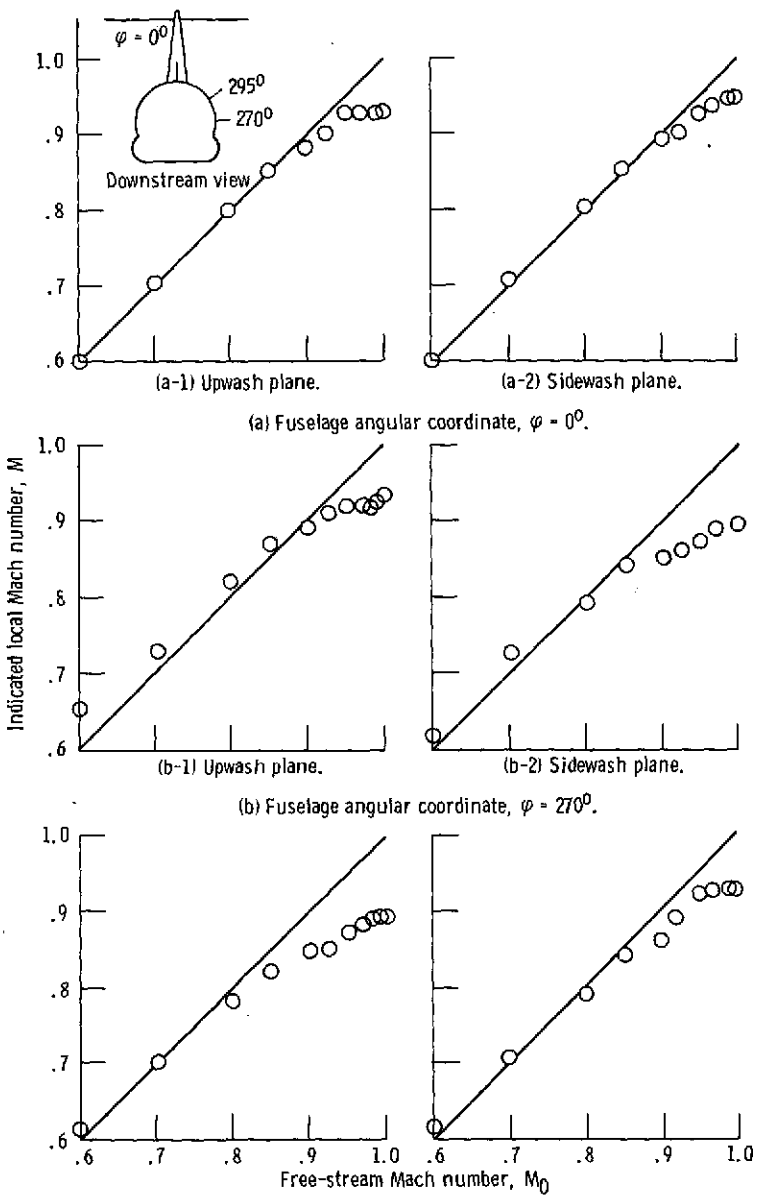

(a-1) Upwash plane. (a-2) Sidewash plane.

(a) Fuselage angular coordinate, $\varphi = 0^0$.

(b-1) Upwash plane. (b-2) Sidewash plane.

(b) Fuselage angular coordinate, $\varphi = 270^0$.

(c-1) Upwash plane. (c-2) Sidewash plane.

(c) Fuselage angular coordinate, $\varphi = 295^0$.

Figure 22. - Measured Mach number at probe face. Model angle of attack, $\alpha = 3.2^0$.

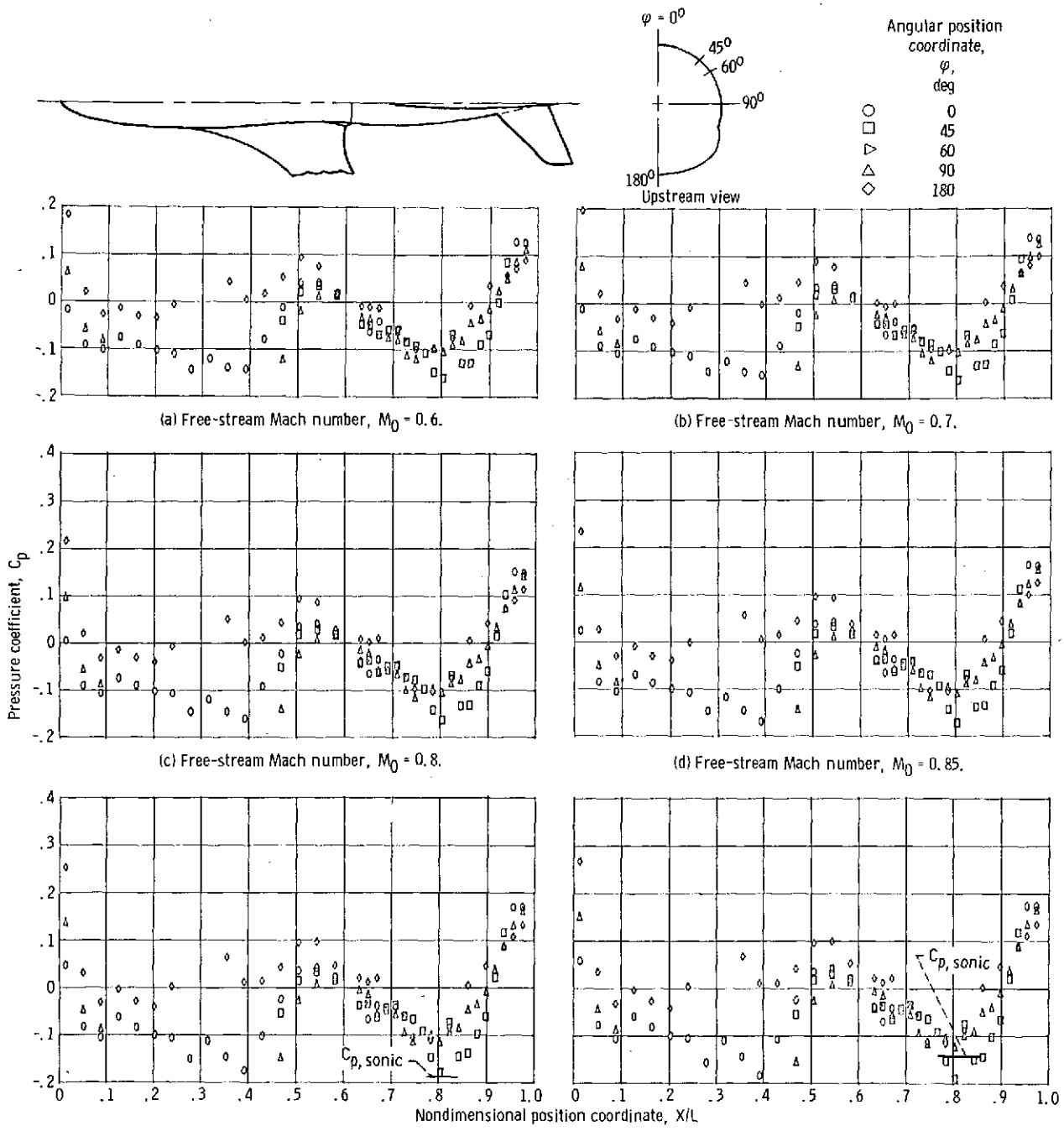

(a) Free-stream Mach number, $M_0 = 0.6$.

(b) Free-stream Mach number, $M_0 = 0.7$.

(c) Free-stream Mach number, $M_0 = 0.8$.

(d) Free-stream Mach number, $M_0 = 0.85$.

(e) Free-stream Mach number, $M_0 = 0.9$.

(f) Free-stream Mach number, $M_0 = 0.92$.

Figure 23. - Effect of free-stream Mach number on reference fuselage pressure distributions at model angle of attack, $\alpha = 3.2^0$.

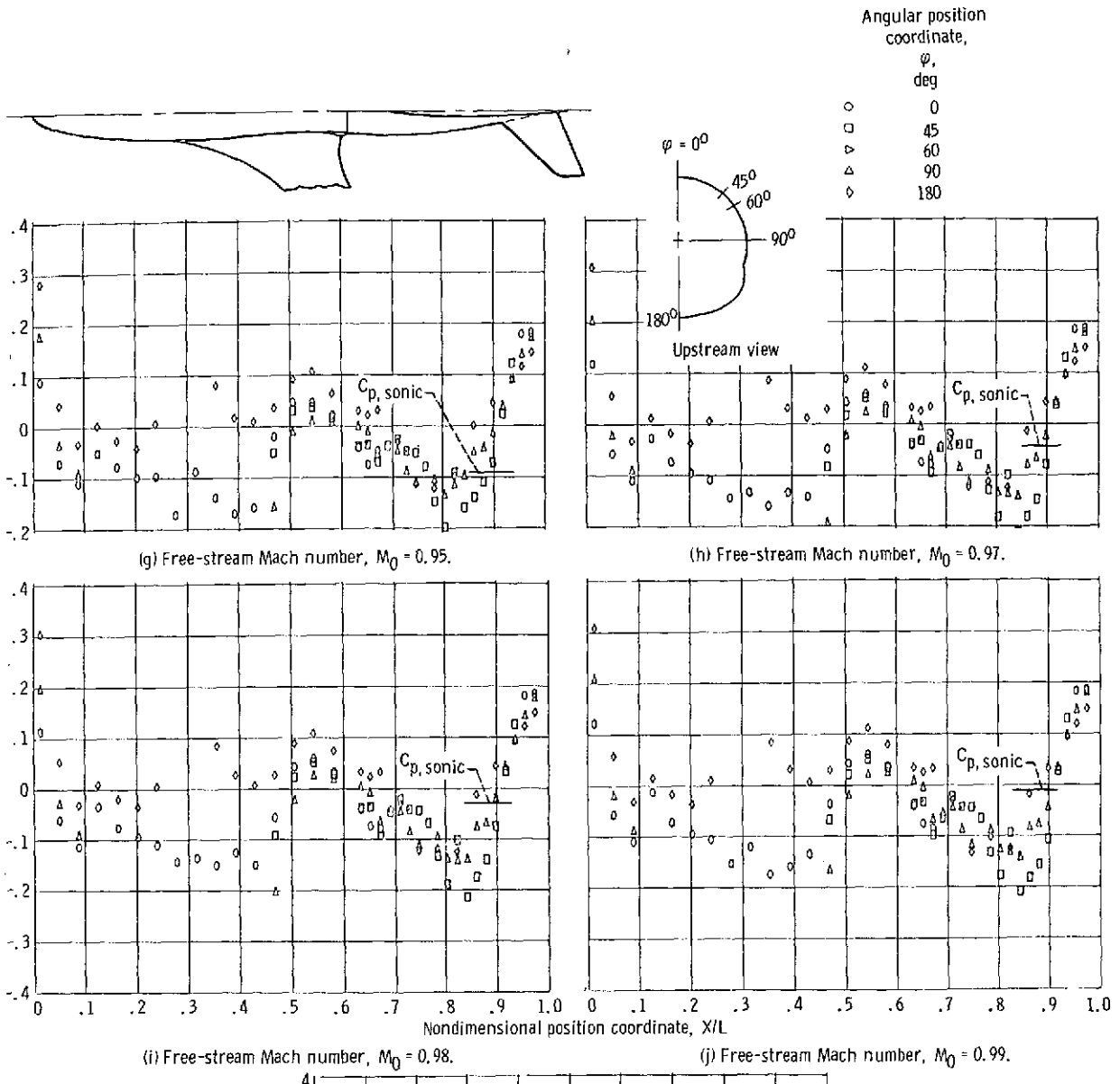

(g) Free-stream Mach number, $M_0 = 0.95$.

(h) Free-stream Mach number, $M_0 = 0.97$.

(i) Free-stream Mach number, $M_0 = 0.98$.

(j) Free-stream Mach number, $M_0 = 0.99$.

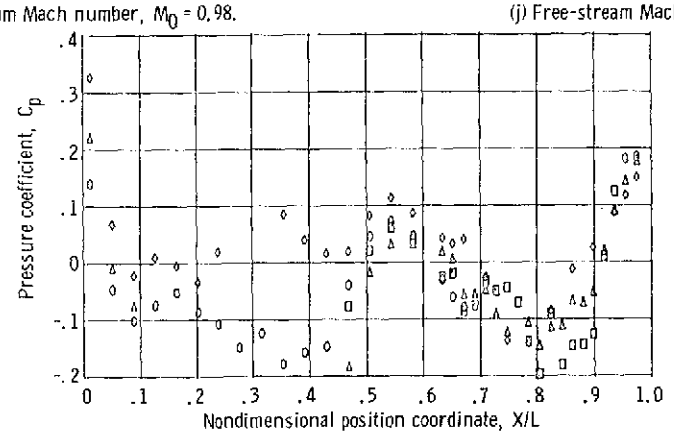

(k) Free-stream Mach number, $M_0 = 1.00$.

Figure 23. - Concluded.

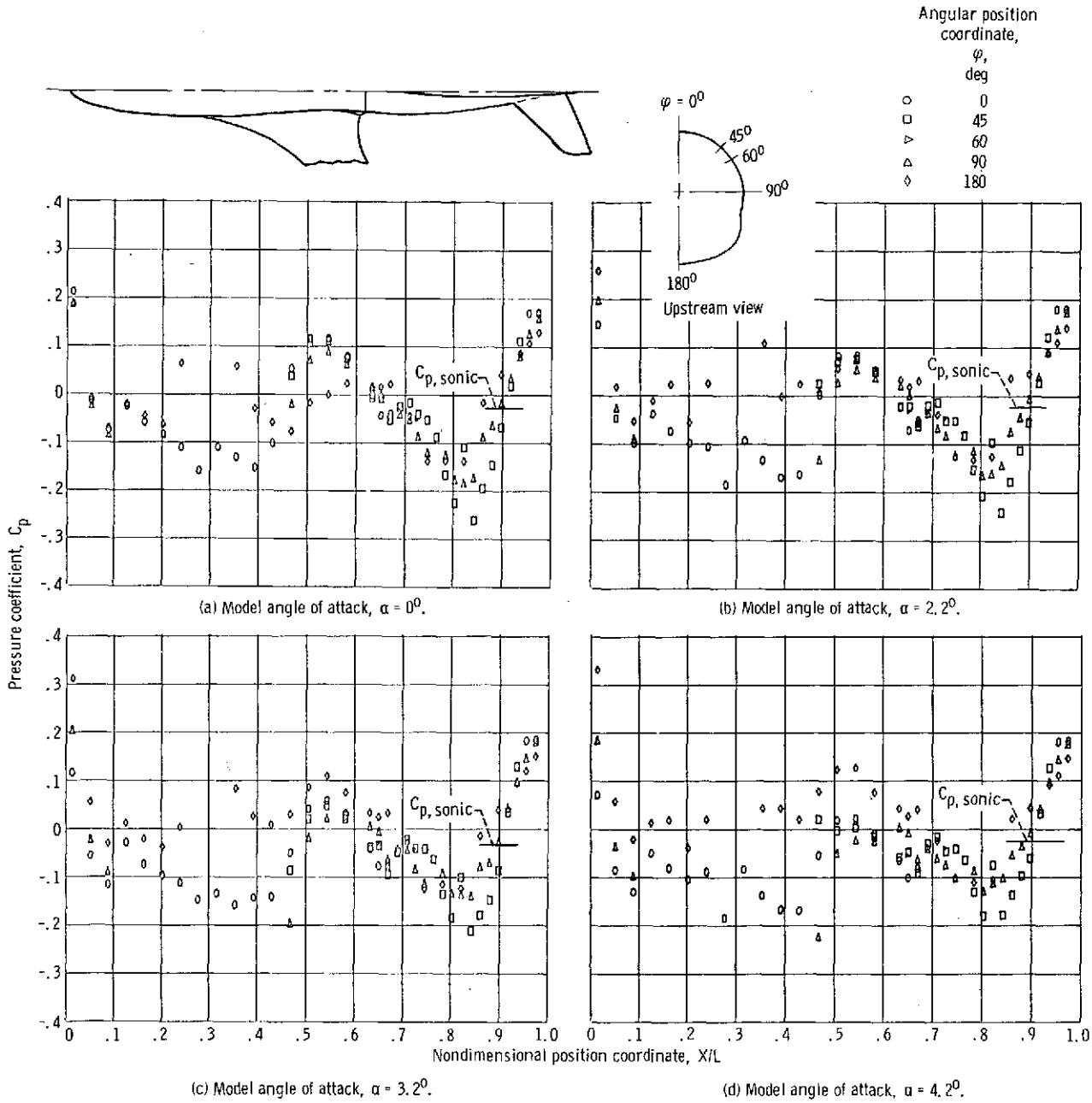

(a) Model angle of attack, $\alpha = 0^{0}$.

(b) Model angle of attack, $\alpha = 2.2^{0}$.

(c) Model angle of attack, $\alpha = 3.2^{0}$.

(d) Model angle of attack, $\alpha = 4.2^{0}$.

Figure 24. - Effect of model angle of attack on reference fuselage pressure distributions at free-stream Mach number, $M_0 = 0.97$.

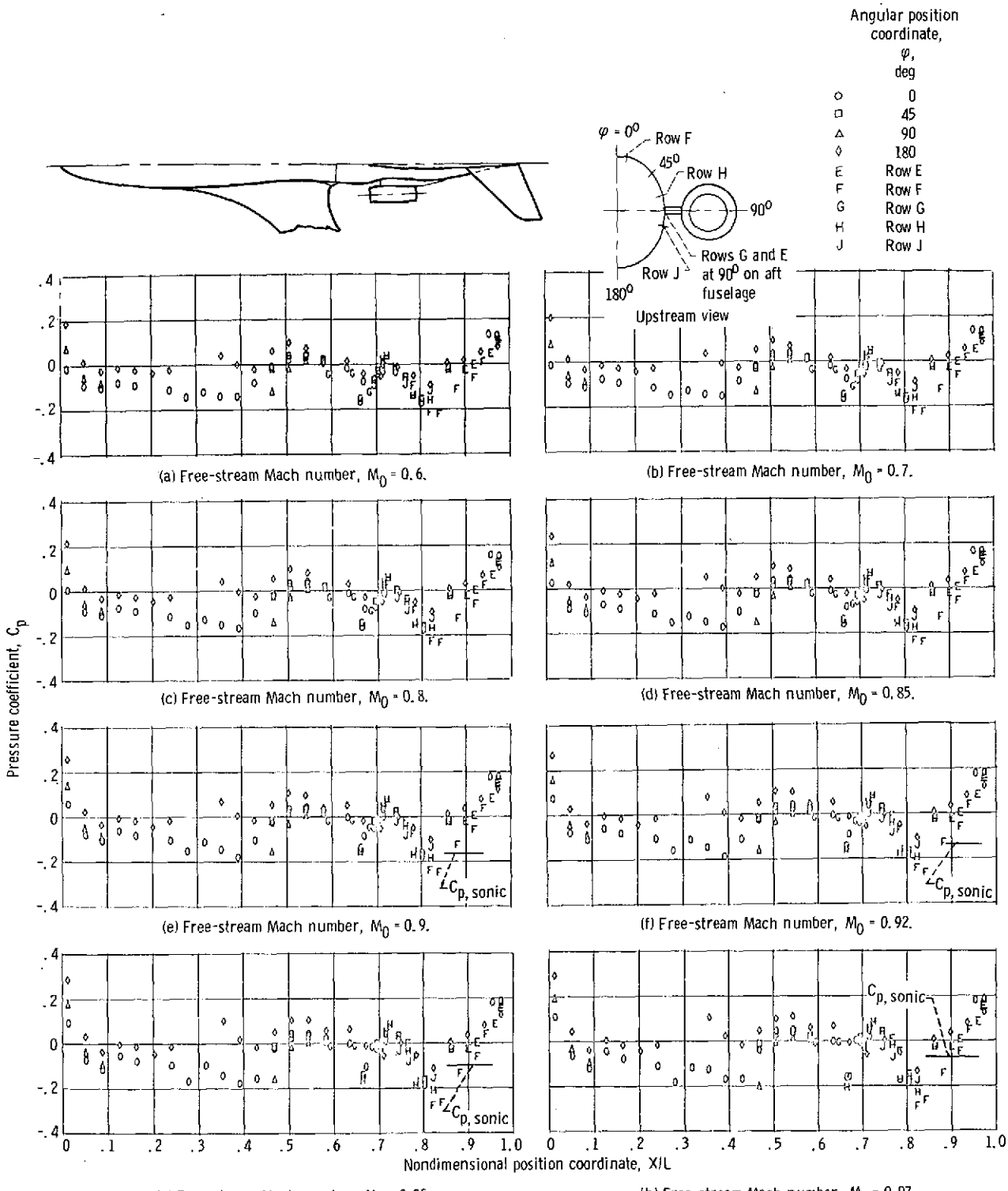

(a) Free-stream Mach number, $M_0 = 0.6$.

(b) Free-stream Mach number, $M_0 = 0.7$.

(c) Free-stream Mach number, $M_0 = 0.8$.

(d) Free-stream Mach number, $M_0 = 0.85$.

(e) Free-stream Mach number, $M_0 = 0.9$.

(f) Free-stream Mach number, $M_0 = 0.92$.

(g) Free-stream Mach number, $M_0 = 0.95$.

(h) Free-stream Mach number, $M_0 = 0.97$.

Figure 25. - Effect of free-stream Mach number on fuselage pressure distributions with flow-through nacelles at model angle of attack, $\alpha = 3.2^0$. NACA-1 inlet contour; nacelle simulated mass flow ratio, $m/m_0 = 0.6$.

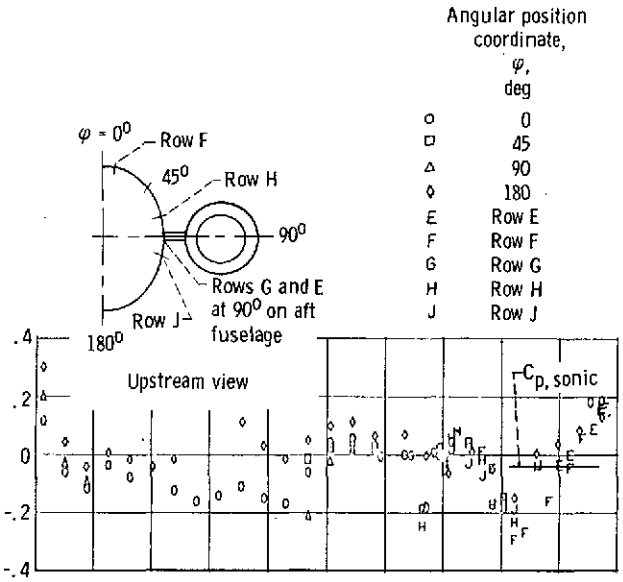

(i) Free-stream Mach number, $M_0 = 0.98$.

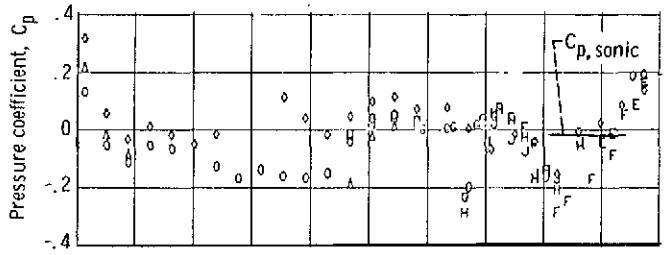

(j) Free-stream Mach number, $M_0 = 0.99$.

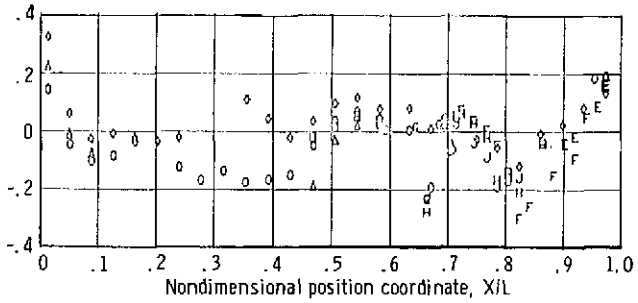

(k) Free-stream Mach number, $M_0 = 1.00$.

Figure 25. - Concluded.

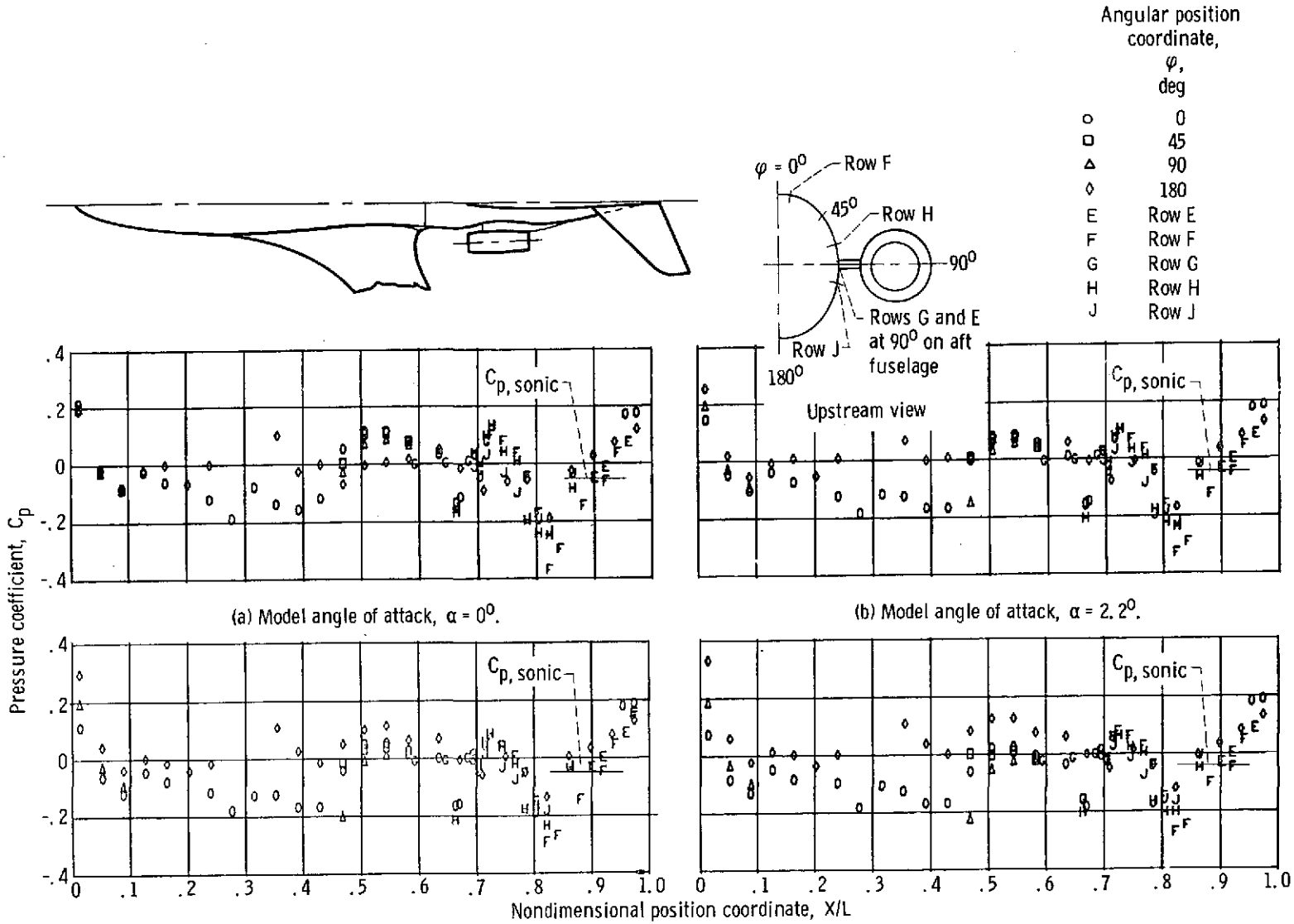

(a) Model angle of attack, $\alpha = 0^{o}$.

(b) Model angle of attack, $\alpha = 2.2^{o}$.

(c) Model angle of attack, $\alpha = 3.2^{o}$.

(d) Model angle of attack, $\alpha = 4.2^{o}$.

Figure 26. - Effect of model angle of attack on fuselage pressure distributions with flow-through nacelles at free-stream Mach number, M_0 = 0.97. NACA-1 inlet contour; nacelle simulated mass flow ratio, m/m_0 = 0.6.

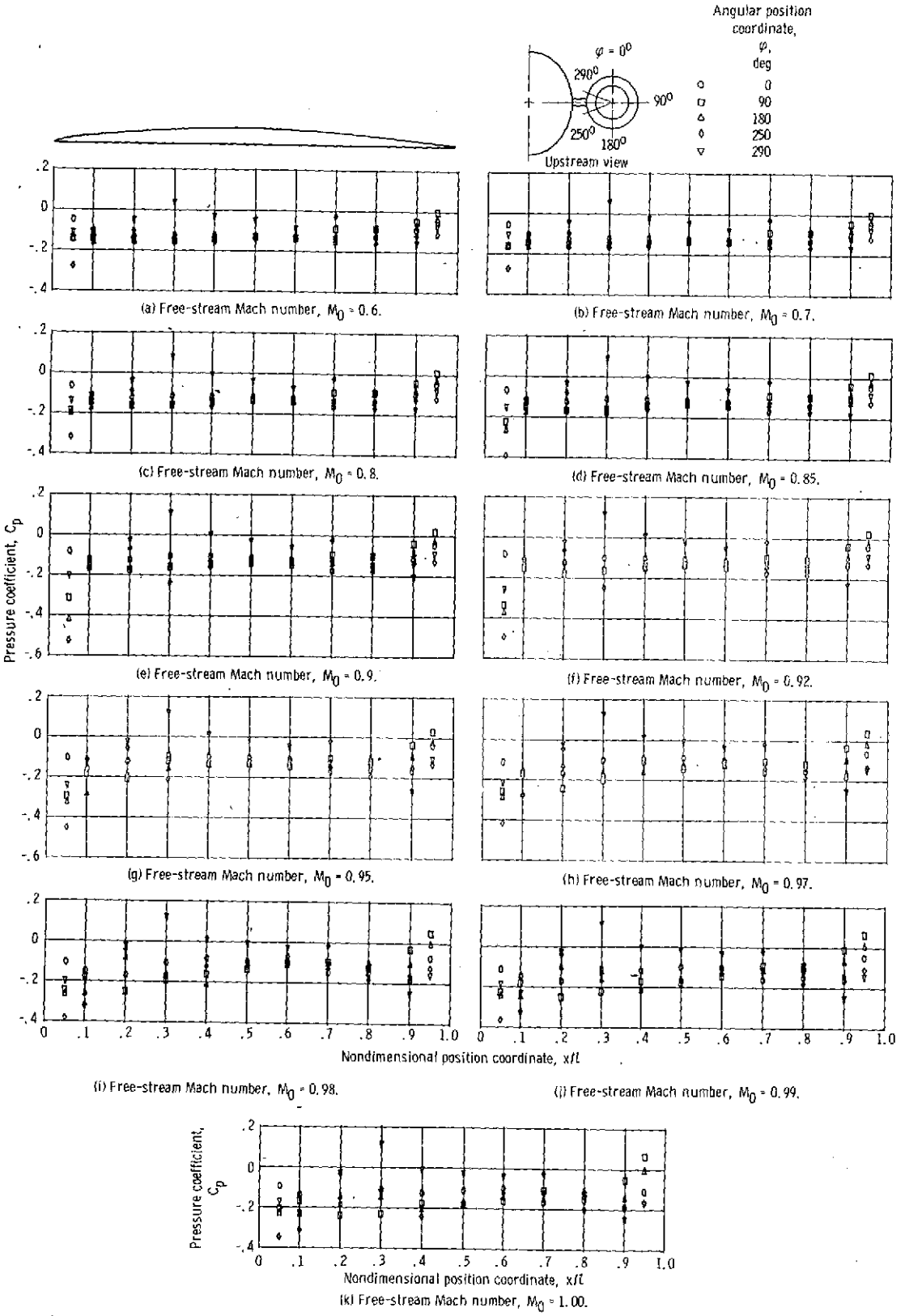

Figure 27. - Effect of free-stream Mach number on nacelle pressure distributions with NACA-1 inlet contour; nacelle simulated mass flow ratio, m/m_0 = 0.6; and model angle of attack, α = 3.2°.

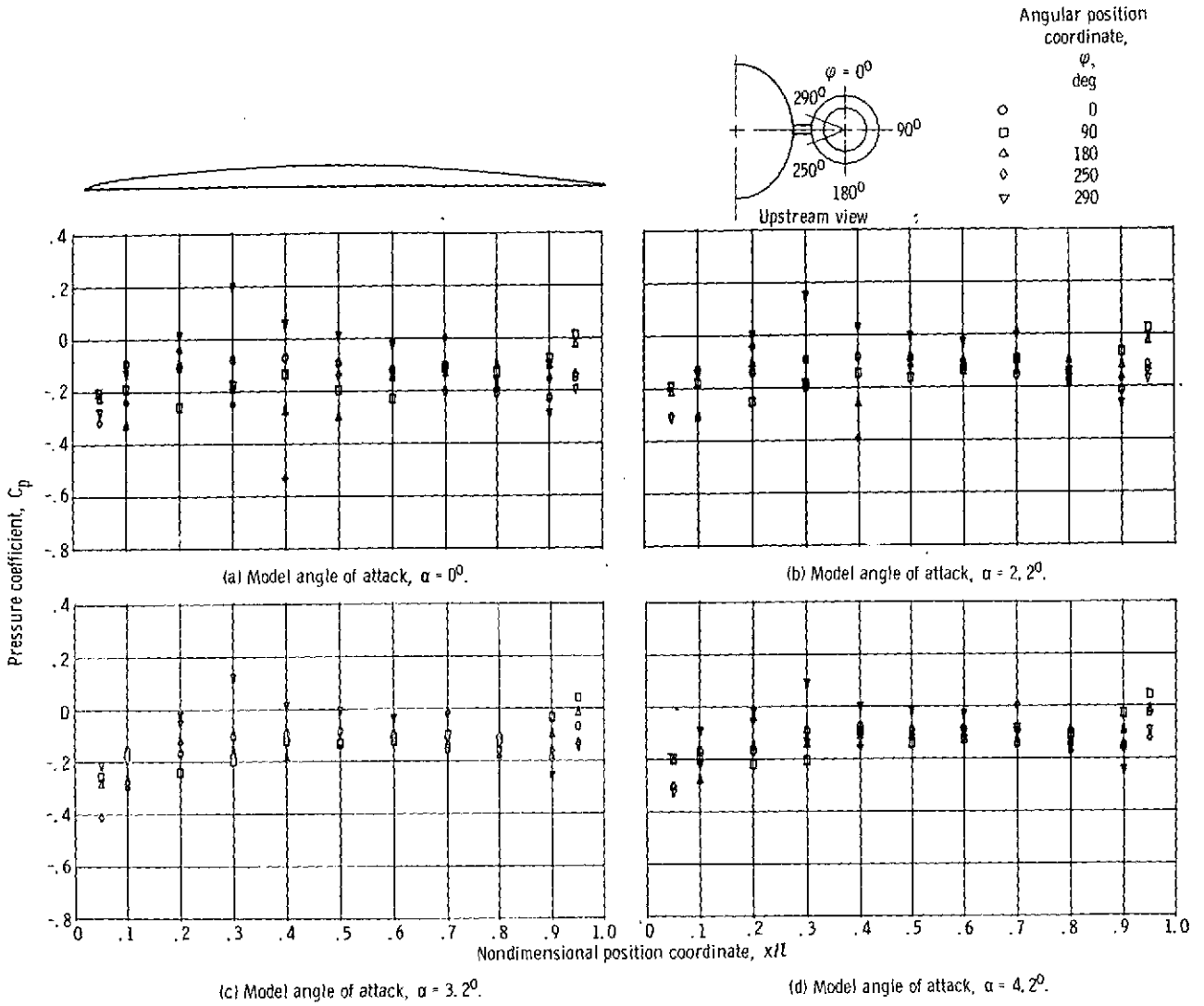

Figure 28. - Effect of model angle of attack on nacelle pressure distributions with NACA-1 inlet contour; nacelle simulated mass flow ratio, $m/m_0 = 0.6$; and free-stream Mach number, $M_0 = 0.97$.

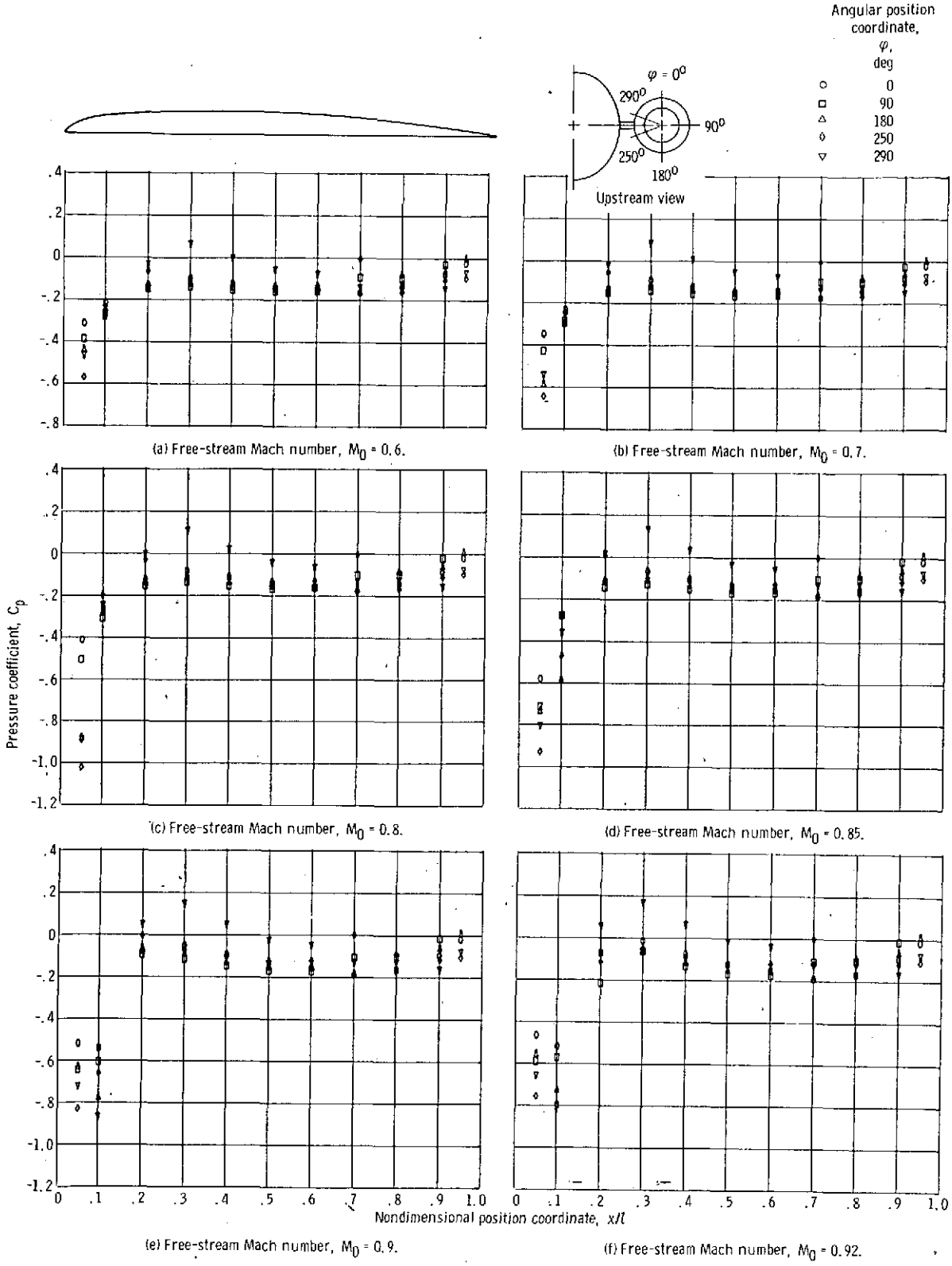

Figure 29. - Effect of free-stream Mach number on nacelle pressure distributions with supercritical inlet contour; nacelle simulated mass flow ratio, m/m_0 = 0.46; and model angle of attack, α = 3.2°.

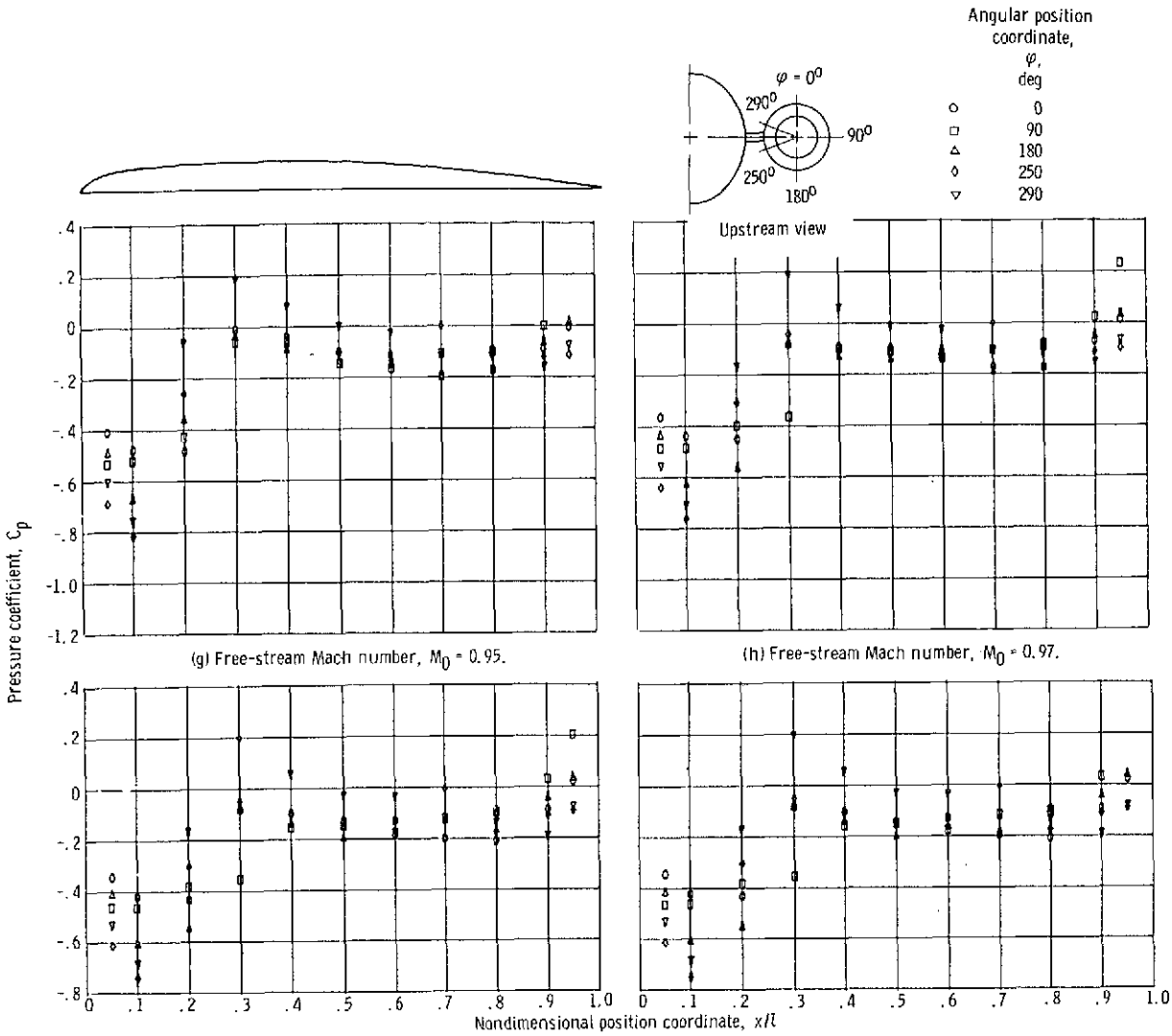

(g) Free-stream Mach number, M_0 = 0.95.

(h) Free-stream Mach number, M_0 = 0.97.

(i) Free-stream Mach number, M_0 = 0.98.

(j) Free-stream Mach number, M_0 = 0.99.

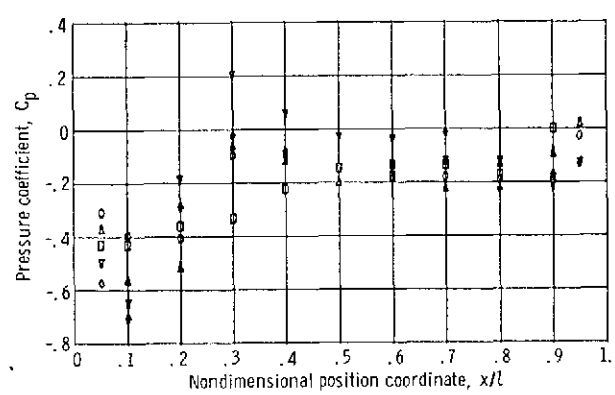

(k) Free-stream Mach number, M_0 = 1.00.

Figure 29. - Concluded.